

## Fatigue crack growth behavior of Ni-Cr-Mo-V steel welded joints considering strength mismatch effect

Wei Song<sup>1\*</sup>, Ping Wang<sup>2</sup>, Di Wan<sup>3</sup>, Guian Qian<sup>4</sup>, José Correia<sup>5,6</sup>, Filippo Berto<sup>3</sup>

1. School of Mechanical & Electrical Engineering, Xuzhou University of Technology, Xuzhou 221018, PR China.
2. School of Ocean Engineering, Harbin Institute of Technology, Weihai 264209, China.
3. Department of Mechanical and Industrial Engineering, Norwegian University of Science and Technology (NTNU), Richard Birkelands vei 2b, 7491 Trondheim, Norway.
4. State Key Laboratory of Nonlinear Mechanics, Institute of Mechanics, Chinese Academy of Sciences, Beijing 100190, China.
5. Institute for Sustainability and Innovation in Structural Engineering, University of Coimbra, 3030-790 Coimbra, Portugal.
6. Institute of R&D in Structures and Construction, University of Porto, 4200-465 Porto, Portugal.

### Abstract:

High strength steel welded joints are usually fabricated by heterogeneous weld metal for reducing the negative impacts of microstructural characteristics and defects on mechanical properties, such as hydrogen embrittlement cracking, joint toughness decreasing, etc. To reflect material heterogeneity in the mechanical characteristics, two kinds of weld filler material are selected to obtain Evenmatched Welded Material (E-WM) and Undermatched Welded Material (U-WM) marine Ni-Cr-Mo-V steel welded joints. The Fatigue Crack Growth (FCG) behaviors of Base Metal (BM) and related welded joints are investigated considering load ratio (0.1, 0.4, 0.7) and specimen state (as-welded and heat-treated) effects. The experimental FCG trends for BM and weldments have been compared with the trends available in standards. The FCG rate ( $da/dN$ ) results show the U-WM demonstrates higher FCGR curves than BM and E-WM. Additionally, it demonstrates no significant difference about FCGR for E-WM and U-WM under high  $R$ -ratios (0.4 and 0.7). Moreover, both E-WM and U-WM in as-welded state presents higher fatigue crack propagation resistance than in the Post Welded Heat Treatment (PWHT) state. The fracture mechanism of FCG was analyzed according to the fatigue crack trajectory in microstructures and fractography. Transgranular fracture behavior were observed with some secondary particles in E-WM, while the intergranular fracture was exhibited with few tiny secondary microcracks in U-WM.

1  
2  
3  
4  
5  
6  
7  
8  
9  
10  
11  
12  
13  
14  
15  
16  
17  
18  
19  
20  
21  
22  
23  
24  
25  
26  
27  
28  
29  
30  
31  
32  
33  
34  
35  
36  
37  
38  
39  
40  
41  
42  
43  
44  
45  
46  
47  
48  
49  
50  
51  
52  
53  
54  
55  
56  
57  
58  
59  
60  
61  
62  
63  
64  
65

**Keywords:**

10CrNi3MoV steel; fatigue crack growth; welded joints; R-ratio effect; material heterogeneity; mismatch.

**1. Introduction:**

For most heavy-loading engineering welded structures and components, such as mine excavators, truck cranes, ships, and marine structures, High Strength Steel (HSS) or Ultra-High Strength Steel (UHSS) has an increasing demand for improving the structural performance and energy efficiency by structure lightweight realization. Conventional steels contain ferrite microstructure, whereas some advanced HSS have microstructure comprised of different phases, such as ferrite, bainite, austenite, and martensite [1-4]. However, welding processing for HSS or UHSS is sensitive to hydrogen embrittlement, even at a relatively low hydrogen concentration [5]. The welded joints made by HSS or UHSS have a considerable risk of delayed fracture. The hydrogen-assisted fracture in HSS depends significantly on the final weldment microstructure [4, 6-8]. Thus, the interaction between the hydrogen and phase constituents of HSS under different conditions is critical to reveal the hydrogen embrittlement mechanism [5]. Since austenite microstructure is prone to giving a higher hydrogen solubility and more hydrogen trapping sites than ferrite microstructure, the austenite consumable is an effective solution for hydrogen-assisted cracking of post welding for HSS or UHSS.

Except for clarifying the hydrogen-assisted fracture mechanism in HSS, some specific treatments are needed to avoid the hydrogen embrittlement fracture for HSS welded joints. Two methodologies were generally adopted to enhance the hydrogen embrittlement resistance by reducing or replacing the precipitates of grain boundary ferrite and intragranular ferrite, which tend to prejudice the mechanical properties of base metal [9, 10]. One strategy is to improve the welding processing to decrease the welding cooling rate, such as decreasing the heat input energy by increasing the welding passes [11], preheating [12], and Post Welding Heat Treatments (PWHT) [13]. Another strategy is to replace the ferrite wires from austenite welding wire with higher hydrogen solubility. The essential mechanism of austenitic filler for the HSS grades is based on the considerable hydrogen trapping sites. However, due to the differences in mechanical properties

1 between dissimilar microstructures, the fabrication by austenite welded joints would seriously  
2 influence the component structural capability compared with ferritic welded joints. Thus, it is crucial  
3 to investigate the underlying mechanical properties of HSS considering welding material  
4 mechanical heterogeneity, especially under cyclic loading. Nevertheless, the fatigue crack  
5 propagation behavior of welded joints is also an excellent performance for overall integrity  
6 reliability. The research of high strength steel fatigue and its weldment properties becomes one of  
7 the significant issues for material mechanical properties assessment.

8  
9  
10  
11  
12  
13  
14 According to the investigations of FCG of weldments, it tends to exert more excellent fatigue  
15 crack propagation resistance for the microstructures composed of acicular ferrite [14]. It can be  
16 attributed that this formed constituent with high angle grain contours can deflect and block the crack  
17 growth, which needs a higher energy demand and enhances the fatigue threshold consequently [15,  
18 16]. In the literature, there are many studies about FCG behavior of HSS welding joints (Q345qD  
19 steel [15], 10Ni5CrMoV steel [17], 25Cr2NiMo1V steel [18], NiCrMoV rotor steel [19], X100 steel  
20 [20], DP780 dual-phase steel [21], WNQ570 [22], S690 [23] and S960 [24]) at different conditions  
21 (Heat input effect [10], welded-repaired state [25], high-pressure hydrogen gas environment [20]  
22 and seawater environment [26]) and different welding processes (Gas Metal Arc Welding (GMAW)  
23 [17], Submerged Arc Welding (SAW) [10], Tungsten Inert Gas (TIG) [21], Laser shock processing  
24 [27]) On the other hand, Wang et al. investigated the FCG behavior of Ni-Cr-Mo-V high strength  
25 steel welded joint considering the effects of residual stresses, stress ratio and specimen thickness  
26 [17]. The results revealed that the acicular ferrite packet weldments have higher fatigue crack  
27 growth resistance than 10Ni5CrMoV steel with tempered sorbite microstructure. Given the  
28 technical limitations of the high strength-toughness welded consumables, a feasible strategy is to  
29 sacrifice the strength to intense the toughness and finally form the undermatched welded joints. The  
30 undermatch effect of S960QL welded joints on FCG behavior has also been studied considering the  
31 specimen orientations [24]. According to the statistics of Paris-Erdogan exponents ( $m$ ) for  
32 overmatched, evenmatched, and undermatched cases, the FCG resistance of overmatched cases is  
33 lower than that of evenmatched cases. In comparison, the FCG resistance of the evenmatched  
34 condition is lower than that of the undermatched condition.

35  
36  
37  
38  
39  
40  
41  
42  
43  
44  
45  
46  
47  
48  
49  
50  
51  
52  
53  
54  
55  
56  
57  
58 Paris and Erdogan proposed the linear relationship of Fatigue Crack Growth Rate (FCGR) and  
59 the Stress Intensity Factor (SIF) range as a double logarithmic scale. As one of the significantly  
60  
61  
62  
63  
64  
65

1 effective factors for weldments, stress ratio  $R$  effect on the fatigue near-threshold and crack stable  
2 growth stages has been widely surveyed considering residual stress. The effect of residual stress  
3 regarding as external secondary stress can be incorporated into the  $R$  ratio to illustrate the fatigue  
4 crack growth behavior. However, the Paris equation cannot directly depict the  $R$  ratio effect; more  
5 corrections of this equation are conducted using two-parameters models [28-30] or crack closure  
6 models [17, 31-33]. Up to now, these two methods have been extensively applied to correlate crack  
7 growth data for different materials, service conditions or loading levels. The emphasis is on which  
8 physical mechanism is suitable for the fracture behavior illustrations and test data correlations.  
9

10  
11 On the other hand, the remained residual stress after manufacturing processes of Compact  
12 Tension (C(T)) welded specimens exhibits significant effects on the FCGR. The quantitative  
13 analysis of residual stress effect on FCGR has been discussed by a combined neutron diffraction  
14 experimental and numerical study for S355 structural steel HAZ [34]. It reveals that the residual  
15 stresses play a vital role in the FCG behavior of welded structures, especially near the fatigue crack  
16 threshold region. The residual stress effect on FCG behavior is more complicated due to the  
17 explicitly stress redistribution in the crack propagation processing. Regarding to the size effect on  
18 FCG behavior, it has not yet been clearly illustrated by experimental evidences, although the content  
19 of plasticity can be used to explain some FCGR results with size variations limitedly [35]. The size  
20 effect on FRCG is supported by the fatigue crack growth investigation of C(T) specimens made by  
21 Inconel-718 alloy [36]. Additionally, Forth, Newman and Forman found that the FCG behavior in  
22 C(T) is strongly supported dependent on the size configurations of thickness and width [37]. The  
23 net-section-based fracture mechanics approach was proposed to characterize the unique specimen-  
24 size correlation of FCGR data of single-edge-cracked specimens. It also found that the geometric  
25 correction factors of fracture mechanics are not adequate to deal with the apparent specimen-size  
26 effects [35].  
27  
28  
29  
30  
31  
32  
33  
34  
35  
36  
37  
38  
39  
40  
41  
42  
43  
44  
45  
46  
47  
48

49  
50 Despite some investigations on fatigue crack growth behaviors of steel weldments under  
51 different conditions, few studies have been done earlier on the fatigue resistance and crack growth  
52 rates characterization of strength mismatch welded joints. In our previous study, the low cycle  
53 fatigue behaviors of 10CrNi3MoV steel and its undermatched weldments have been investigated  
54 [38]. To clarify the residual life of related welded components by fracture mechanics theory, the  
55 present work focuses on the FCG behavior of 10CrNi3MoV steel welded joints produced by GMAW  
56  
57  
58  
59  
60  
61  
62  
63  
64  
65

1 considering the material heterogeneity effect. Firstly, the material microstructure, tensile properties,  
2 and fatigue crack growth were analyzed in detail. The FCGR and related standard codes of base  
3 metal and weldments were discussed to assess fatigue crack propagation resistance under the as-  
4 welded and PWHT states. Subsequently, fatigue crack propagation mechanisms were examined  
5 based on the optical microscope and scanning electronic microscopy (SEM) observations of crack  
6 growth paths and crack surfaces. Finally, the primary conclusions were summarized. This study  
7 provides useful experimental data for safe designs and life prediction considering the material  
8 heterogeneity effect.  
9

## 10 11 12 13 14 15 16 17 18 **2. Materials and experimental methods**

### 19 20 21 22 **2.1. Materials and welding processing**

23  
24  
25  
26 10CrNi3MoV low alloy high strength steel is typically used in shipbuilding and submarine  
27 structures with the excellent comprehensive performance of strength and ductility, which has a yield  
28 strength of about 700 MPa. Two different filler materials were chosen to manufacture the butt-  
29 welded joints. The chemical compositions of base metal (BM), evenmatched, and undermatched  
30 filler materials are given in Table 1. Evenmatched butt welded joint with a V-groove was fabricated  
31 by Single Pulsed Gas Metal Arc Welding (SP-GMAW) processing by corresponding wire (wire  
32 diameter  $\Phi$  1.2 mm) in 12 mm sheet. While Gas Metal Arc Welding (GMAW) processing was  
33 performed to obtain undermatched welded joints by filling lower strength weld metal (wire diameter  
34  $\Phi$  1.2 mm). Multipass butt-welded joints are prepared with double V-grooved design as displayed  
35 in Fig. 1, which is taken into account of back-chipping processing. For both evenmatched and  
36 undermatched weldments, eleven depositions were carried out to fill the prepared groove. The  
37 GMAW welding heat input and torch moving speed were controlled as 0.7-0.85 KJ/mm and 4.5-5.3  
38 mm/s. During the joining process, the interpass temperature was maintained under 80 °C between  
39 the passes to avoid the hot cracking [38]. The related welding parameters of butt joints were given  
40 in Table 2.  
41  
42  
43  
44  
45  
46  
47  
48  
49  
50  
51  
52  
53  
54  
55  
56  
57  
58  
59  
60  
61  
62  
63  
64  
65

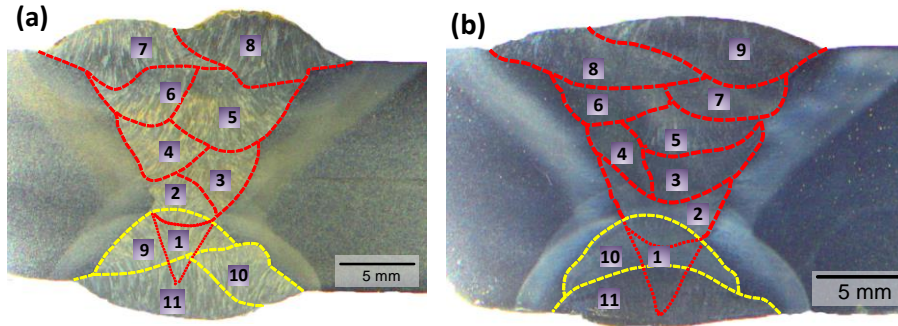


Fig. 1. The multipass butt welded joints schemes considering the back-chipping processing. (a) Evenmatched welds, (b) Undermatched welds.

Table 1. Nominal chemical composition of the BM and undermatched weldments (%) [38].

Steel	C	Si	Mn	Cr	Mo	Ni	Cu	V	S	P
10CrNi3MoV /Evenmatched- Welds	0.09	0.29	0.48	0.94	0.4	2.88	-	0.06	0.005	0.011
Undermatched- Welds	0.027	0.243	1.3	0.051	-	1.09	0.05	-	0.0073	0.011

Table 2. Welding parameters of E-WM and U-WM butt joints [38].

Current (A)	Voltage (V)	Welding speed mm/s	Electrode diameter mm	Shielding gas 80% Ar- 20% CO <sub>2</sub> L/min	Heat input (KJ/mm)	Interpass temperature °C
140- 190	24-28	4.5-5.3	1.2	20	0.7-0.85	<80

## 2.2. Monotonic tensile and microhardness tests

The monotonic tensile tests of base metal and weldments were conducted by using a universal testing machine under the strain rate  $2 \times 10^{-3}/s$  at room temperature. A servo-hydraulic strength machine MTS 809 was used for the tests. To evaluate the deformation of specimens, the strain was measured by a linear variable extension meter connected to an amplifier. The tests were aimed at determining the strength characteristics of BM and filler materials.

Microhardness tests were performed on the polished multi-pass welded specimens using a Vickers hardness tester at a load of 500 g and dwell time of 10 s. To avoid any potential effect of strain fields developed by adjacent indentations, adequate distance (400  $\mu m$ ) was spaced between consecutive indentations. These hardness measurements of undermatched and evenmatched welds were conducted along a cross line from welds.

### 2.3. FCGR experimental methods

Compact Tension (CT) specimens for FCGR tests were cut by Electron Discharge Machining (EDM) from base metal and welded plate along the parallel welding direction to a width of  $W = 62.5$  mm following ASTM E647 standard. The weld pads of approximate dimensions  $500 \times 400 \times 16$  mm<sup>3</sup> were prepared, and the shape and dimension of specimens are depicted in Fig. 2. Noted that the CT specimens were extracted from the center of welded plate, and the final thickness  $B$  of CT specimens was fabricated to 8 mm. Moreover, initial crack length  $a_0$  was taken as 20mm. The Given fatigue crack initiation direction along with weld bead, the orientation of the notch tips of CT specimens was parallel to weld bead. To obtain stabilized microstructure and reduce the potential residual stress effect on FCGR results, Post-Welding Heat Treatment (PWHT) at 550 °C for 4 h and cooling in the furnace was carried on for BM specimens and most of the welded specimens. Finally, the FCG behaviors of heterogeneity materials considering different states were compared and analyzed.

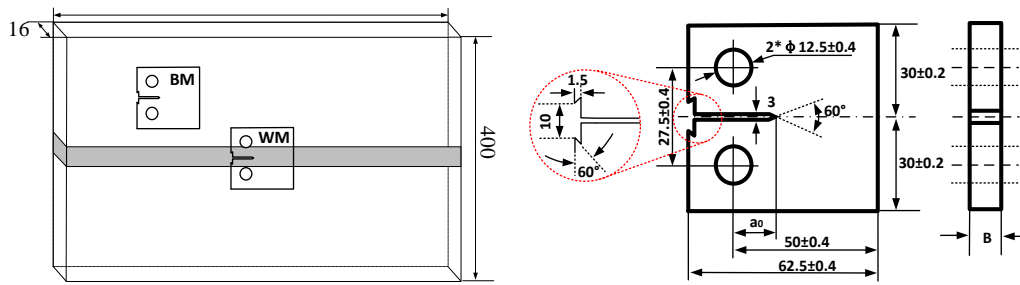


Fig. 2. Fatigue crack growth sample illustration. (a) Schematic diagram of CT specimens from weld plate (mm); (b) Geometry of CT specimens (mm).

FCGR tests were conducted at room temperature on an Instron 8802 electro-hydraulic servo testing system. The load capacity of the machine is 25 tons for both tension and compression. The CMOD measuring system based on the compliance method is applied to obtain the FCG rates by accessional fracture extensometer. All the specimens were tested under a constant amplitude sinusoidal loading under three load ratios ( $R = 0.1, 0.4, \text{ and } 0.7$ ) at a constant frequency of 10 Hz. It should be noted that the frequency has negligible effects on the FCG behavior of steel materials in the air environment [26]. The fatigue propagation crack length was measured continuously by a crack mouth clip gauge based on the compliance method. After the FCGR tests, fatigue crack paths and fracture surfaces were observed by SEM. Before FCG testing, a 3 mm fatigue pre-crack was

1 produced from the notch for CT specimens using the  $K$ -decreasing procedure as suggested in [39].  
2 The crack lengths were measured by the compliance method by a highly sensitive Instron 15 mm  
3 axial extensometer. The gauge pins were placed in the notches of the CT specimen. The notch  
4 geometry details were presented in Fig. 3(b). It should be noted that a lower bound threshold SIF  
5 range between 15 and 20 MPa·m<sup>0.5</sup> was used to initiate the crack. Additionally, the final crack length  
6 of stopping test was set as 25 mm.  
7  
8  
9  
10  
11  
12

## 13 **2.4. Microstructure characterization**

14  
15  
16  
17 Post-mortem fractographic characterization was conducted to understand the microstructural  
18 and fracture appearance difference on tested specimens by Optical Microscope (OM) and Scanning  
19 Electron Microscope (SEM). The FEG Quanta 650 SEM (Thermo Fisher Scientific Inc., USA) was  
20 operated at 20 kV acceleration voltage with an aperture size of 50 μm. Crack profiles were examined  
21 by Electron Back Scatter Diffraction (EBSD) system. The samples with fatigue cracks were ground  
22 a 2000 grit SiC paper followed by polished using a colloidal silica suspension (OP-S, Struers).  
23 Besides, the quantitative information from fracture surfaces was obtained using the built-in software  
24 on the cross-section of the specimen. For microstructural analysis, samples were etched with Nital  
25 reagent (96 ml ethyl alcohol and 4 ml HNO<sub>3</sub>) for 45 s.  
26  
27  
28  
29  
30  
31  
32  
33  
34  
35  
36

## 37 **2.5. Residual stress measurements**

38  
39  
40 As a destructive technique, the Hole-Drilling (HD) strain gauge method was employed to  
41 measure the welding residual stress distributions on the top surface of multipass butt welded joints.  
42 A milling processing is conducted to obtain a smooth surface for the measurements of residual stress  
43 distribution around the weld joints. Note that a slow milling speed is utilized to avoid additional  
44 residual stress during this processing. After the milling process, electro-chemical corrosion is  
45 conducted on the newly-formed surface to remove some milling traces. The dimension of three-  
46 element strain-gauge rosettes is 11 mm × 11 mm with a 5 mm diameter of gauge circle. The drilled  
47 hole diameter is 1.5 mm, and the drilled hole depth is about 2 mm. The calculation of longitudinal  
48 and transverse residual stresses was conducted by related equations on the basis of the measured  
49 relieved strain.  
50  
51  
52  
53  
54  
55  
56  
57  
58  
59  
60  
61  
62  
63  
64  
65



### 3. Results

#### 3.1 Results of monotonic tensile tests

Fig. 3 shows the monotonic stress-strain curve of base metal and weldments under the strain rate  $2 \times 10^{-3}/s$ . It can be seen from the figure that the T (the ultimate tensile strength) / Y (0.2% proof yield strength) ratio of 10CrNi3MoV steel reaches 1.07, which indicates that the capability of base metal for hardening is limited. The T/Y ratio of undermatched welds is higher than the base metal, which reaches 1.12. In this Figure, BM, E-WM, and U-WM represent Base Metal, Evenmatched Weldments, and Undermatched Weldments, respectively. Table 3 gives the mechanical properties comparisons of these materials under monotonic tension loading. The curves of BM and E-weld reveal a better performance than undermatched weld in terms of yield strength and tensile strength with the values about 710 MPa and 750 MPa. The yield strength and tensile strength of U-weld is lower than other materials, which is about 498 MPa and 559 MPa. Good ductility for U-weld and E-weld can be observed according to the comparison of fracture strain from the tensile curves, while the base metal exhibits bad ductility (fracture strain <10%).

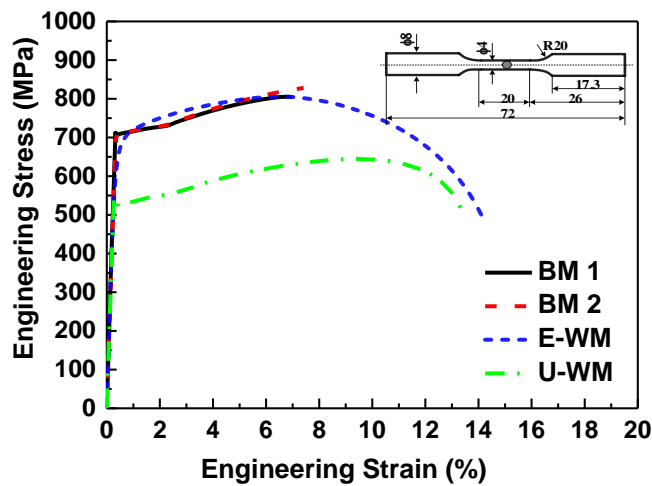


Fig. 3. Monotonic stress-strain curves of 10CrNi3Mov high strength steel and its undermatched welds.

Table 3. Mechanical properties of test materials.

Steel	Yield strength (MPa)	Tensile strength (MPa)	Young's modulus (GPa)	Poisson's ratio	Elongation at fracture	Kv (J) -20°C
BM (10CrNi3MoV)	710	750	205	0.3	7.6%	275
E-WM	693	741	205	0.3	14.2%	280

### 3.2. Microstructure and hardness profiles

The tested microstructures of 10CrNi3MoV high strength steel as Base Metal (BM), Evenmatched weldment (E-WM), and Undermatched weldment (U-WM) by OM and SEM equipment are presented in Fig. 4. These micrographs illustrate the grain boundaries and the non-uniform distribution of precipitates by optical microscope and SEM analyses. The BM showed in Fig. 4(a) (d), which is quenched and tempered, has a fine microstructure mainly composed of Acicular Ferrite (AF), tempered Martensite (M), and Granular Carbides (GC) from metallographic observations. The fast-cooling rate in E-WM further resulted in AF and Bainite (B) grains. Grain boundary Ferrite (GF) also can be seen in the E-WM. Conversely, it was observed that the microstructures in U-WM contain mainly ferrite, partially melted grains with notable pearlite, and precipitation of carbides formed in the grain boundaries. It should be noticed that inclusions in E-WM can contribute positively to nucleation acicular ferrite, which has a positive role in improving the toughness and fatigue strength of the weld [22].

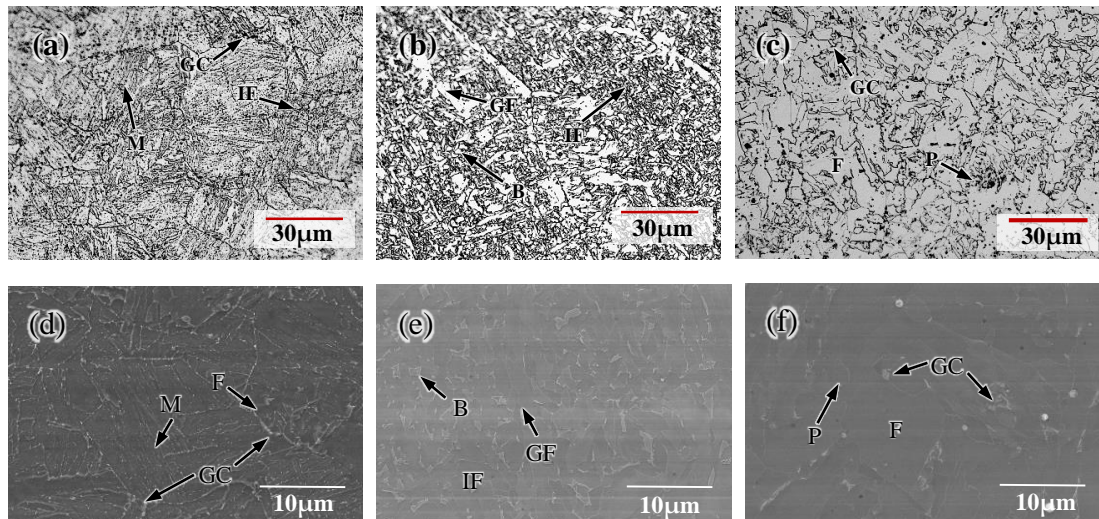


Fig. 4 Optical micrographs (a), (b), (c), and scanning electron microscopy (SEM) figures (d), (e), (f), of BM, E-WM, and U-WM, respectively. Note: AF-Acicular Ferrite, GF-Grain Boundary Ferrite, IF-Intragranular Ferrite, M-Martensite, GC-Granular Carbides, and P-Pearlite from metallographic observations.

Fig. 5 shows the hardness variations of fusion zone and HAZ for weldments along the transverse section of the E-WM and U-WM welded joints before PWHT. As presented in Fig. 5(a), the soften

zone occurs in E-WM welds, which implies that the microhardness of this area is slightly lower than that of base metal. The Coarse Grain HAZ (CGHAZ) covered the area at approximately 2 mm near the fusion zone demonstrated the highest hardness, in which the averaged hardness value of this area is about 350 HV. It implies that the harder martensite phase microstructures than the base metal exist in CGHAZ. It also infers that the Solid-State Phase Transformation (SSPT) occurs during the welding processes. Similar observations are also exhibited in Fig. 5(b). During the welding process, the fusion zone and HAZ experience fast heating and cooling cycle in an extremely short time. The peak temperature of weldments exceeds the melting point, which results in liquidation, solidification, and solid-phase changes. The final hardness of welded joints and corresponding HAZ is determined by its chemical composition and cooling conditions. The HAZ hardness of E-WM welds is comparative with that of U-WM welds. It should be noted that the hardness of E-WM fusion zone is higher than the base metal after welding. According to U-WM plots, it is evident a very pronounced reduction in microhardness at the fusion zone of U-WM due to dissimilar weld filler with base metal, which reaches about 180 HV. The non-uniform distributions of the alloy components, composition, and morphology of welding metal led to a non-uniform distribution of hardness at the welded joint [40]. The non-uniform microstructure distributions also influence fatigue crack growth behaviors of materials.

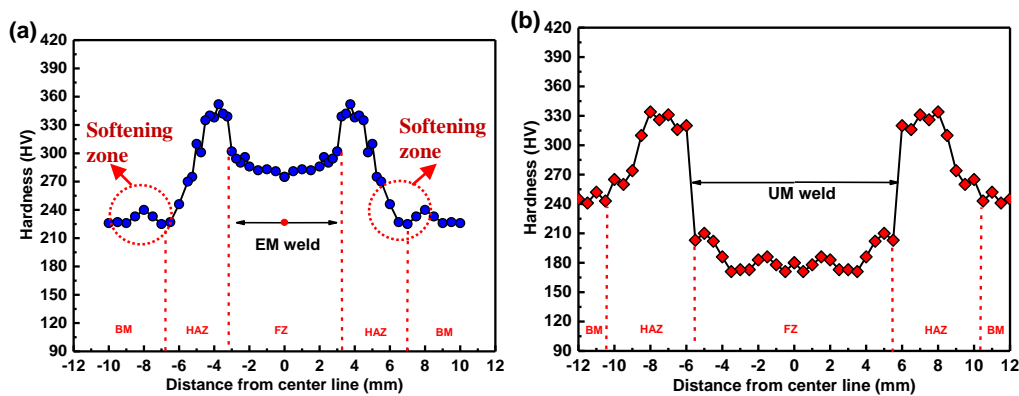


Fig. 5 The hardness distributions of evenmatched welds (a) and undermatched welds (b).

### 3.3. Residual stress distribution in welded joints

The welding residual stress induced have a significant influence on the FCGR of welded joints or components. It is necessary to explore the stress contributions of high strength steel welded joint considering the weldment properties, especially for different mismatch welded joints. On the one

1 hand, the mismatch weldment may exert smaller tensile residual stress magnitudes, which make the  
2 changing of structural capacity. On the other hand, the stress can be modified from the tensile state  
3 to compressive state due to the SSPT effect, which further prolong the fatigue life of weld  
4 components. Additionally, the FCGR curves under the as-welded and PWHT state can be illustrated  
5 by the stress distributions. Generally, the tensile residual stress will accelerate the FCGR and the  
6 compressive residual stress will redundant the fatigue crack propagation. Although parts of residual  
7 stresses may be released in small-scale specimen, they play an important role on fatigue behavior  
8 and should be considered in design purposes [41]. In order to completely perceive the influence of  
9 residual stresses on FCGR behavior, it is essential to consider state of residual stresses during the  
10 welding processing, and the redistribution state with the growth of fatigue crack if there is not  
11 releasing residual stress.

12  
13  
14  
15  
16  
17  
18  
19  
20  
21  
22  
23 The longitudinal and transverse residual stresses were simulated according to the E-WM and U-  
24 WM material thermal-mechanical properties, which is presented in Fig. 6. In the figure, the LS  
25 stands for the residual stress of longitudinal direction, while the TS represents the residual stress of  
26 transverse direction. It should be noted that the E-WM and BM will occur the SSPT during the  
27 multipass welding. The residual stress in welded joints were calculated with and without the  
28 consideration of the SSPT behavior. According the presented results in Fig. 8, the SSPT behavior  
29 has a crucial influence on the state and magnitudes of residual stress for both welded joints. In the  
30 Fig. 6(a), the high tensile residual stress for the longitudinal direction occurs in the E-WM joint  
31 without the SSPT effect. While the transverse residual stress in the weld center tended to be in a  
32 compressive state. Since the SSPT behavior modifies the distribution of residual stress in the E-WM  
33 joints, the tensile stress zones in longitudinal and transverse directions were transferred from the  
34 weld surface to the inside. Significantly, the surface passes in the E-WM joint can induce the  
35 apparent compressive residual stress. The residual stress of U-WM joints is shown in Fig. 6(b), the  
36 SSPT behavior of BM in U-WM joints seems has no obvious effect on the residual stress due to the  
37 small part subjected to high temperature.

38  
39  
40  
41  
42  
43  
44  
45  
46  
47  
48  
49  
50  
51  
52  
53  
54 The longitudinal stress is crucial for the FCG behavior on the basis of the extracted direction of  
55 C(T) specimens. The comparisons between experimental and calculated residual stress for the E-  
56 WM and U-WM are conducted and exhibited in Fig. 7. The calculated residual stresses considering  
57 the SSPT behavior in E-WM joint demonstrate more accurate estimations than the results without  
58  
59  
60  
61  
62  
63  
64  
65

1 considering SSPT behavior in Fig. 7(a). The simulated residual stresses in U-WM joint in Fig. 7(b)  
 2 make good agreements with the experimental data no matter whether the SSPT procedure is  
 3 involved into the computations.  
 4  
 5

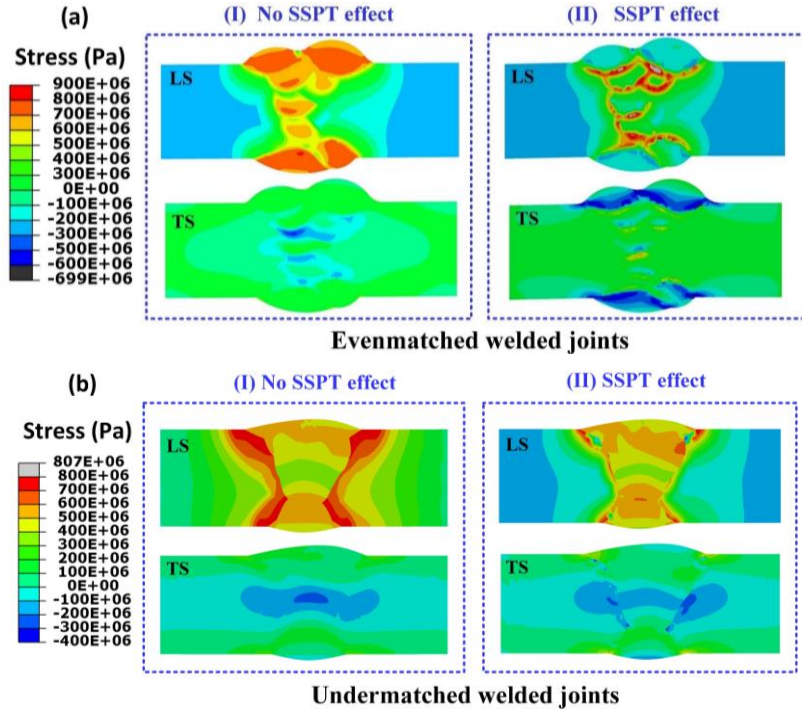


Fig. 6. The residual stress contours considering SSPT effect for evenmatched (E-WM) and undermatched (U-WM) welded joints.

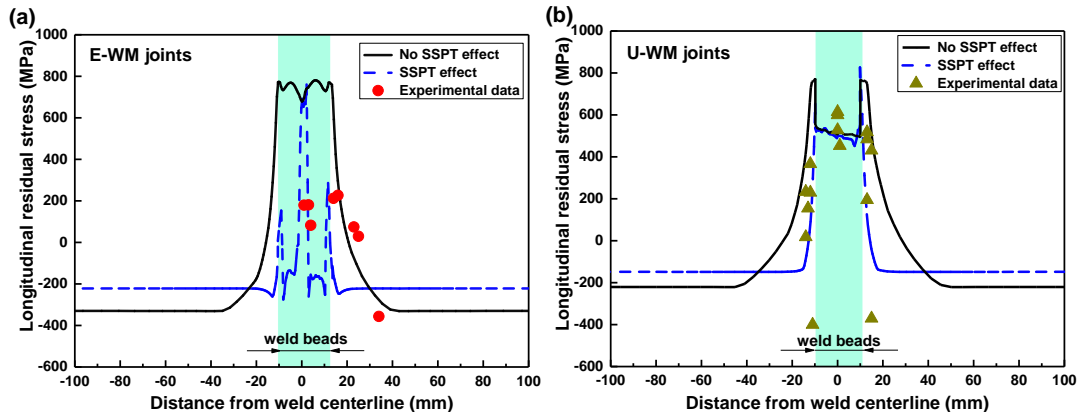


Fig. 7. The residual stress results comparisons between the FE models and experimental data for E-WM and U-WM joints in longitudinal directions. (a) Longitudinal stress in E-WM joint, (b) Longitudinal stress in U-WM joint.

### 3.4. Fatigue crack growth behavior

Given the linear log-log relationship  $da/dN$  and  $\Delta K$ , a fatigue crack growth trend can be divided

1 into three regions. (i) Region I represents the threshold stage before the fatigue crack growth, which  
 2 is characterized as  $\Delta K_{th}$ . It means that no crack propagation can be detected when the applied  $\Delta K$  is  
 3 below the fatigue crack threshold value. (ii) Region II is the fatigue crack growth domain stage. (iii)  
 4 Region III stands for the final fatigue crack growth accelerating stage. Generally, Region II can be  
 5 quantitatively described by the Paris law:  
 6  
 7  
 8  
 9

$$10 \quad da / dN = C \cdot \Delta K^m \quad (1)$$

11 where  $a$  represents the crack length, and  $N$  is the number of the cycles, giving  $da/dN$  the discrete  
 12 crack extension/growth per cycle.  $C$  and  $m$  are material constants in specific testing conditions,  
 13 while  $\Delta K$  is the range of the SIF experienced by the material during the fatigue cycles. Generally,  
 14 the  $\Delta K$  ranges in the measuring machine are calculated using the formula proposed in ASTM E647  
 15 for CT specimens:  
 16  
 17  
 18  
 19  
 20  
 21

$$22 \quad \Delta K_I = \frac{\Delta P}{B\sqrt{W}} \cdot \frac{(2 + \alpha)}{(1 - \alpha)^{3/2}} (0.886 + 4.64\alpha - 13.32\alpha^2 + 14.72\alpha^3 - 5.6\alpha^4) \quad (2)$$

23 Where  $\alpha = a/W$ ,  $a$  is the crack size,  $B$  is the thickness of the specimen,  $W$  is the specimen width, and  
 24  $\Delta P$  is the applied load range. Regarding crack growth rate  $da/dN$ , it can be computed by the seven-  
 25 point incremental polynomial technique based on the ASTM E647 standard. Furthermore,  
 26 regression analysis is conducted under logarithmic coordinates, and FCGR parameters in terms of  
 27 Paris law can be derived from the relationships between  $da/dN$  and  $\Delta K$ .  
 28  
 29  
 30  
 31  
 32  
 33  
 34  
 35  
 36

37 According to the BS7910 standard [39], the FCG behavior of a metallic material in Region II,  
 38 including the base metal and weldments, can be described by two formulations: a simplified Paris  
 39 law and a two-stage Paris law. The difference between the simplified and two-stage Paris laws lies  
 40 in the specific characteristic stages. The simplified law mainly clarifies the FCG behavior of Region  
 41 II, while the two-stage Paris law presents the Region I and Region II stages with different reference  
 42 line slopes considering the existence of threshold values for base metal and welds. Though the two-  
 43 stage Paris law gives a more conservative reference line for FCGR than the simplified Paris law, it  
 44 is convenient to facilitate the comparison procedure with experimental results by the simplified  
 45 Paris law in our study. The related parameters are collected in Table 4. On the other hand, similar  
 46 reference lines have also been recommended from IIW standards [42]. According to the  
 47 recommended parameters from IIW and BS7910, the Paris law parameters for BM and WM are  
 48 given differently. Furthermore, IIW and BS7910 guidelines of the Paris law curves as reference  
 49  
 50  
 51  
 52  
 53  
 54  
 55  
 56  
 57  
 58  
 59  
 60  
 61  
 62  
 63  
 64  
 65

curves are used to compare with experimental results in the following figures, which are determined with a high survival probability and for a high confidence level. The simplified Paris-law constants for mean curves recommended by BS7910 and IIW for BM and weldments in the air environments were summarized in Table 5. In the table, two types of  $\Delta K$  units are given for power-law constants, m/cycle and mm/cycle, respectively.

To demonstrate the crack growth behavior of materials without considering the residual stress effect, the FCGR as a function of the crack length for base metal and weldments under as-welded and PWHT states at  $R=0.1$  was plotted in Fig. 8. An exponential linear tendency of these materials results was observed. Fig. 8(a) shows the curves of FCGR versus crack length under an as-welded state for three different materials. It shows that the initial crack length is about 13 mm after pre-cracking. The FCGR of E-WM is evidently lower than that of BM and U-WM with the fatigue crack increases. However, the FCGR values among these three materials under the PWHT state in Fig. 8(b) are comparative at the beginning of the crack growth. With the propagation of crack length, the FCGR values of BM and E-WM are also lower than that of U-WM, which implies that the BM and E-WM have stronger fatigue crack growth resistance.

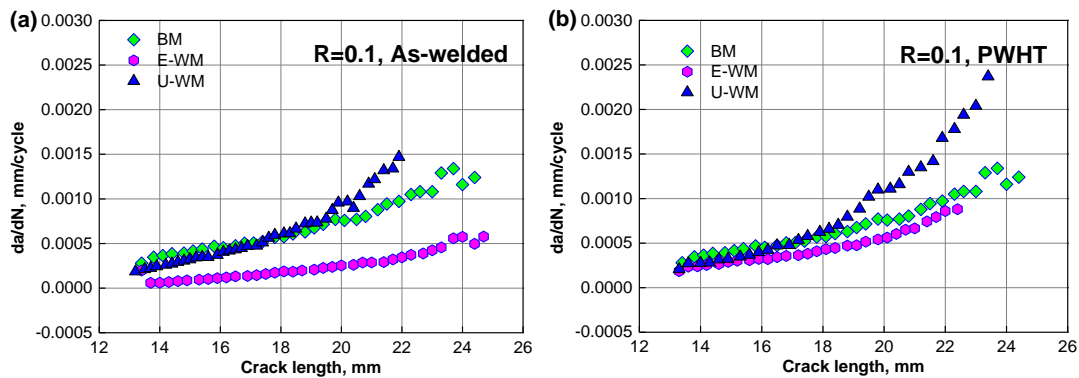


Fig. 8 Fatigue crack growth rate as a function of crack length. (a) the As-welded state, (b) the PWHT state.

The FCGR curves of base metal and weldments (E-WM and U-WM) at stress ratio  $R=0.1$  are plotted in Fig. 9. The FCGR comparisons between as-welded and PWHT states were conducted for these three materials. As presented in Fig. 9(a), the FCGR of BM isn't influenced by the PWHT processing, which means no residual stress effect on FCGR in BM. The FCG data on the BM are compared with the simplified Paris-law reference lines recommended by BS7910 and IIW in Fig. 9. Although the FCGR data were not fitted by the linear relationship in the log-log axes, the discrepancy between the experimental data and IIW or BS7910 recommended lines can be observed

1 obviously. Due to the high survival probability and for a high confidence level for the recommended  
2 curves, the FCGR results of BM are significantly lower than the BM recommendation data of  
3 simplified law from IIW and BS7910 considering the high confidence level. It further illustrates  
4 that the standard codes can derive a safer fatigue life for welded joints by the fracture mechanics'  
5 approach.  
6  
7  
8  
9

10 In Fig. 9(b), it is notable that the FCGR variation in E-WM specimens is affected by PWHT  
11 processing. The FCGR against the range of the SIFs  $\Delta K$  of as-welded state for E-WM at  $R=0.1$  is  
12 higher than that of the PWHT state. However, the FCGR of E-WM for two different states is lower  
13 than that of BM. It can be seen that from this figure that the FCGR data points fall in below the  
14 simplified curves recommended by both BS7910 and IIW. It suggests that for the range of obtained  
15 SIFs, the simplified Paris-law recommended by the standard codes provide a conservative  
16 estimation of weldment behavior. According to the experimental and calculated residual stress  
17 distribution of E-WM and U-WM, it demonstrates different residual stress states in different  
18 direction. The compressive residual stress in E-WM is shown due to the SSPT during the welding  
19 processing, which is illustrated in the above section. Thus, the improvement of FCG resistance for  
20 E-WM can be attributed to the existence of compressive residual stress. The compressive residual  
21 stress can result in crack closure and further incur the increasing fatigue crack resistance, which is  
22 favorable for the reduction of the SIF range of FCGR [43, 44].  
23  
24  
25  
26  
27  
28  
29  
30  
31  
32  
33  
34  
35  
36

37 By contrast, it was observed that the difference between as-welded and PWHT state for U-WM  
38 seems not significant at  $R=0.1$  in Fig. 9(c). The FCGR under the as-welded state is slightly lower  
39 than the PWHT state. It demonstrates an opposite behavior for weldments, which can be attributed  
40 to the tensile residual stress effect on the fatigue crack growth for weldments. In addition, the FCGR  
41 curves of U-WM under as welded and PWHT occurred intersections partly comparing with the  
42 FCGR curve of BM. A comparison in terms of collected FCGR curves for the BM and the WM (E-  
43 WM and U-WM) was plotted in Fig. 9(d). The overview of FCGR curves for BM and WM are  
44 exhibited clearly. The U-WM for PWHT state seems to be the highest FCGR, and E-WM for the as-  
45 welded state also shows the lowest FCGR. Finally, the Paris constants  $C$  and  $m$  from FCGR curves  
46 under different states for BM and WM were fitted according to the related equations presented in  
47 Table 3.  
48  
49  
50  
51  
52  
53  
54  
55  
56  
57  
58  
59  
60  
61  
62  
63  
64  
65



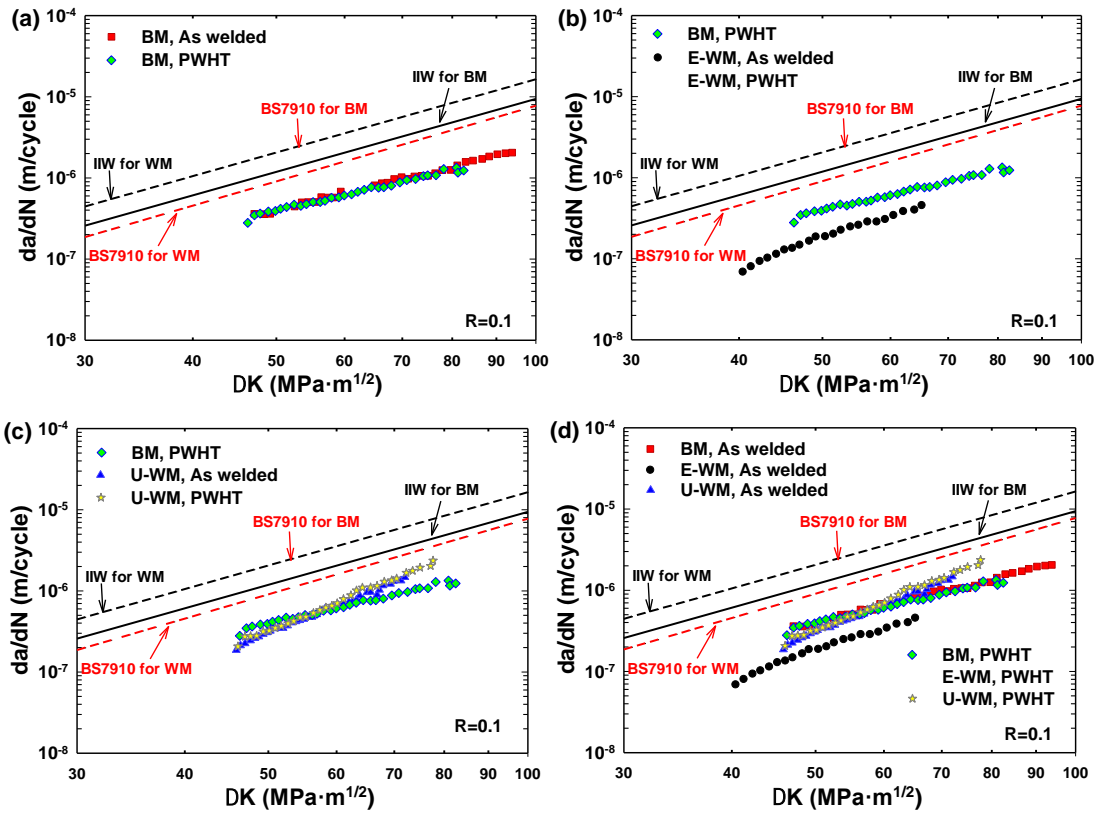


Fig. 9. Effect of specimen state on the FCGR of 10CrNi3MoV steel and its weldments by comparison with standard codes at R=0.1: (a) BM; (b) E-WM; (c) U-WM; (d) Comparison between BM and WM.

Table 4. Summary of the calculated Paris constants for the different FCGR results of base metal and weldments depicted in Fig. 5. (Units:  $\Delta K$  in  $\text{MPa}\cdot\text{m}^{1/2}$ ,  $da/dN$ , in  $\text{m}/\text{cycle}$ )

No.	Stress ratio $R$	$P_{\max}$ (KN)	$P_{\min}$ (KN)	State	$C$	$m$	$s^2$	Average $C$	Average $m$
BM-1	0.1	13.3	1.33	As-welded	$1.24 \times 10^{-11}$	2.65	0.979	$1.24 \times 10^{-11}$	2.65
BM-2	0.1	13.3	1.33	PWHT	$2.64 \times 10^{-11}$	2.46	0.979		
BM-3	0.4	16.7	6.7	PWHT	$4.28 \times 10^{-11}$	2.41	0.948	$4.29 \times 10^{-11}$	2.41
BM-4	0.7	16.7	11.7	PWHT	$5.96 \times 10^{-11}$	2.37	0.937		
E-WM-1	0.1	13.3	1.33	As-welded	$2.13 \times 10^{-13}$	3.49	0.988	$2.13 \times 10^{-13}$	3.49
E-WM-2	0.1	13.3	1.33	PWHT	$4.08 \times 10^{-12}$	2.84	0.943		
E-WM-3	0.4	16.7	6.7	PWHT	$5.28 \times 10^{-11}$	2.37	0.931	$6.32 \times 10^{-11}$	2.45
E-WM-4	0.7	16.7	11.7	PWHT	$1.33 \times 10^{-10}$	2.15	0.967		
U-WM-1	0.1	13.3	1.33	As-welded	$4.74 \times 10^{-14}$	4.01	0.993	$4.74 \times 10^{-14}$	4.01
U-WM-2	0.1	13.3	1.33	PWHT	$1.56 \times 10^{-14}$	4.32	0.993		
U-WM-3	0.4	16.7	6.7	PWHT	$1.07 \times 10^{-11}$	2.78	0.992	$4.49 \times 10^{-12}$	3.47
U-WM-4	0.7	16.7	11.7	PWHT	$2.78 \times 10^{-12}$	3.32	0.987		

Table 5. Simplified fatigue crack growth constants recommended by IIW and BS7910.

Standards	Material	Units	$C$	$m$
<b>IIW</b>	BM	N and mm	$3 \times 10^{-13}$	3
	BM	N and m	$9.487 \times 10^{-12}$	3
	WM	N and mm	$5.21 \times 10^{-13}$	3
	WM	N and m	$1.65 \times 10^{-11}$	3
<b>BS7910</b> (Simplified)	BM	N and mm	$5.21 \times 10^{-13}$	3
	BM	N and m	$1.65 \times 10^{-11}$	3
	WM	N and mm	$1.10 \times 10^{-13}$	3.1
	WM	N and m	$4.91 \times 10^{-12}$	3.1

To quantitatively compare the effects of stress ratio and microstructure on the FCG rate, the experimental investigations for base metal and its weldments under different stress ratios ( $R = 0.1, 0.4, 0.7$ ) are conducted. Fig. 10 shows the FCGR curves of 10CrNi3MoV steel and its weldment specimens tested with load ratio variations. After eliminating the effect of residual stress in CT specimens, the results of CT specimens are compared under the PWHT state. For base metal in Fig. 10(a), the FCGR curve of E-WM is the lowest one compared with BM and U-WM. The FCGR curve of BM is higher than that of E-WM, while the intersection between the BM and U-WM curves occurs due to different Paris law constant  $m$  values. For the low  $R$ -ratio ( $R=0.1$ ), FCGRs in U-WM have lower resistance than that in the BM and E-WM. For the high  $R$ -ratios (0.4 and 0.7), FCGRs of E-WM and U-WM are the same as those of BM in the Paris region, which are presented in Fig. 10(b) and (c). Combined with all tested FCGR curves under different  $R$ -ratios into Fig. 10(d), it presents results comparing FCGRs of BM and WM. Although some articles report that the  $R$ -ratio is insensitivity in some high strength aerospace materials and bridge structural steels, the  $R$ -ratio effects on FCGRs of 10CrNi3MoV steel and its weldments are visible, especially for the E-WM. It also can be observed that FCGRs in the BM and WM become faster as the  $R$  ratios increase, which is consistent with the consensus on the  $R$ -ratio effect for most metallic materials. On the other hand, regarding the weldment heterogeneity effect on FCGRs under high-stress ratio ( $R=0.4$  and  $R=0.7$ ) for E-WM and U-WM, it does not demonstrate an apparent discrepancy with the results of BM.

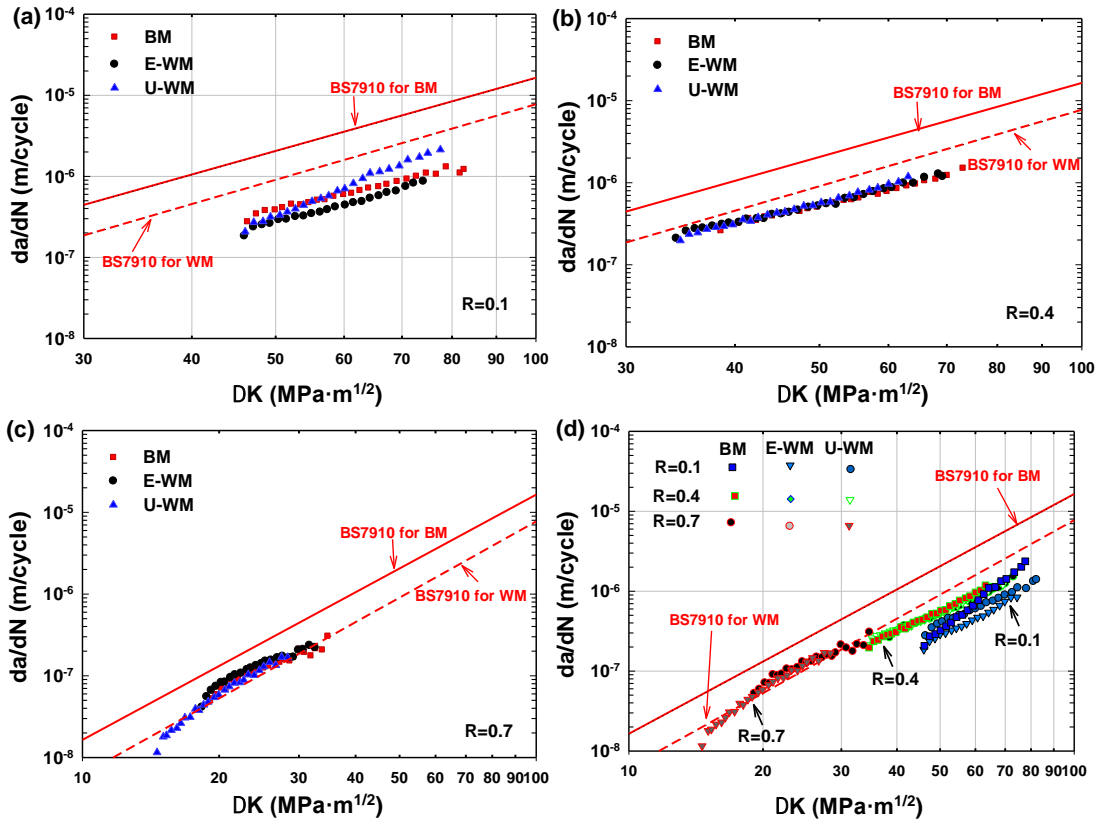


Fig. 10. Effect of stress ratio on the FCGR of 10CrNi3MoV steel and its weldments under PWHT by comparison with standard codes: (a) R=0.1; (b) R=0.4; (c) R=0.7; (d) Summary for different stress ratio.

### 3.5. Fatigue crack growth tests data from the literature

The FCGR data on the CT specimens from 10CrNi3MoV steel and its weldments in the study are compared with the available fatigue test data from the literature on different structural steel grades and the BS7910 standards. More information about the test data in this section is collected in Table 5, such as the microstructure, basic mechanical properties, dimensions, welding processing, and fatigue stress ratios. As shown in Table 5, the data collected from the literature are on different grades of the high strength structural steels. Our study only compared the experimental data of base metal and corresponding weldments at stress ratio  $R=0.1$  to facilitate the assessment procedure. It should be noticed that the simplified recommendation lines from BS7910 for base metal and weldments in the air are employed to compare with the experimental data. The materials used for comparison are SSAB Weldox 960Q steel [26], VOESTALPINE Alform 960M steel [26], S700E steel [26], 10Ni5CrMoV steel [19], S355 steel [25], S690 steel [25], S355G8+M steel [28], DP780 steel [23], Q345qD steel [13], WNQ570 steel [24]. These FCGR data include base metal and its

corresponding weldments, which were mainly tested from CT specimens and part of Single Edge Notched Bending (SENB) specimens. Also, the thickness range is from 1.5 mm to 50 mm for various materials in this study.

In Fig. 11, the FCGR values from the SENB specimens made by SSAB Weldox 960 steel and VOESTALPINE Alform 960M steel are lower than that of CT specimens made by other steels in the initial crack propagation stage, which is attributed to the difference of geometry constraint between the SENB specimens and CT specimens. FCGR data from some base metals (10CrNi3MoV steel and S690 steel) are near the BS7910 recommendation curve. As seen from this figure, the comparison of FCG trends of different steels exhibits some variations of related fracture parameters of Paris law.

On the other hand, the FCG curves of 10Ni5CrMoV steel, S690 steel, and DP780 dual-phase steel are near and below the BM BS7910 recommendation curve. It can be assumed that the universal parameters from BS7910 BM recommendations are adequate for the FCG reference line. By contrast, most FCGR data from different FZ and HAZ falls below the BS7910 recommendation curve of weldments, which illustrates that the simplified recommendation curves from BS7910 are reliable for assessing FCG behavior. To quantify the characteristic of Paris-Erdogan law parameters, the correlation curve is established to reflect the relationship between  $C$  and  $m$  in [26].

Table 5. Specimen specifications, microstructure, and the welding process for different steel grades.

Materials	Area	Microstructure	$\sigma_{YS}$ (MPa)	$\sigma_{UTS}$ (MPa)	Thickness (mm)	Welding process	PWHT	Stress ratio $R$
SSAB Weldox 960Q [26]	BM	-	1030	1076	15	-	-	0.1
	FZ1 (Evenmatched)	-	$\geq 930$	$\geq 980$	15	GMAW	No	0.1
	FZ2 (Undermatched)	-	757	842	15	GMAW	No	0.1
VOESTALPINE Alform 960M [26]	BM	-	1051	1058	15	-	-	0.1
	FZ1 (Evenmatched)	-	$\geq 930$	$\geq 980$	15	GMAW	No	0.1
	FZ2 (Undermatched)	-	757	842	15	GMAW	No	0.1
S700E [26]	BM	-	791	836	15	-	-	0.1
	FZ1 (Evenmatched)	-	$\geq 790$	$\geq 880$	15	GMAW	No	0.1
	FZ2 (Overmatched)	-	$\geq 890$	$\geq 950$	15	GMAW	No	0.1
10Ni5CrMoV [19]	BM	Tempered sorbite	811	864	5, 10	-	-	0.1,0.25,0.4,0.7

	FZ	Martensite, acicular ferrite	613	952	5, 10	TIG	Yes	0.1,0.25,0.4,0.7
S355 [25]	BM	Ferrite, perlite	419	732	8	-	-	0, 0.25
S690 [25]	BM	Needle martensite	766	823	5	-	-	0, 0.25
S355G8+M [28]	BM	Ferrite, perlite	455	544	16	-	-	0.1
	HAZ	-	455	544	16	SAW	No	0.1
DP780 [21]	BM	Martensite, ferrite	546	792	1.5	-	-	0.1
	FZ	Martensite, ferrite	544	749	1.5	TIG	No	0.1
	HAZ	Tempering martensite, ferrite	-	-	1.5	TIG	No	0.1
Q345qD [13]	BM	Ferrite, pearlite	382	556	13.85	-	-	0.1, 0.2, 0.5
	FZ	Bainite, ferrite, pearlite	580	684	13.5	FCAW	No	0.1, 0.2, 0.5
WNQ570 [24]	BM	Ferrite, bainite	495	568	10	-	-	0.1, 0.2, 0.5
	FZ	Bainite, ferrite and pearlite	569	665	10	MCAW	No	0.1, 0.2, 0.5

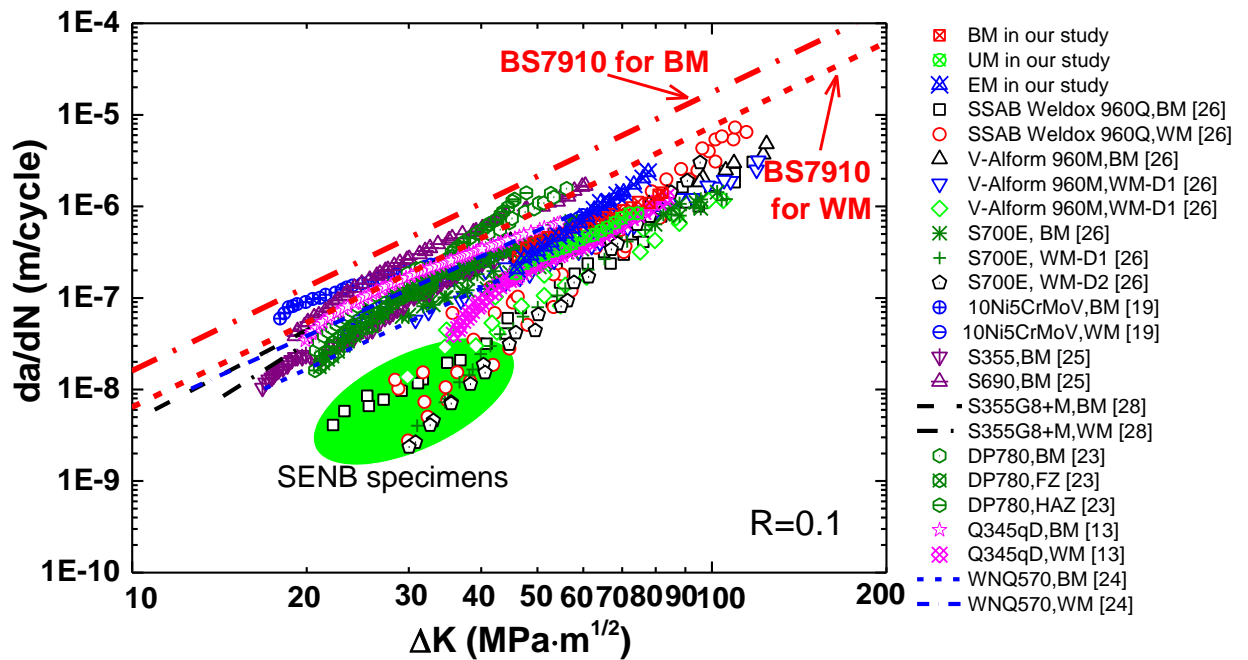
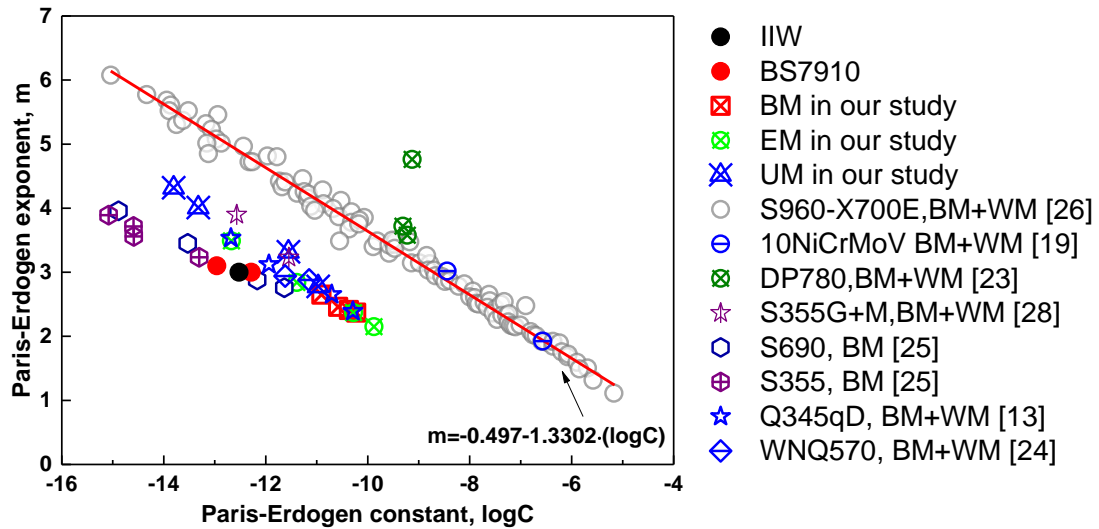


Fig. 11. FCGR on base metal and weldments of structural high strength steel in the air from literature data and BS7910 recommendation curves.

To quantify the Paris-Erdogen parameters from the FCGR data in the above literature, the correlation between  $C$  and  $m$  for SSAB Weldox 960Q, VOESTALPINE Alform 960M, and S700E high strength steel and its mismatched weldments in [26] were established. It is shown in Fig. 12

1 that the logarithmic constant  $C$  and exponent  $m$  values exhibit a great linear relationship. However,  
 2 the experimental data from our study and other literature could not drop into the linear curve in [26],  
 3 and the majority of reference data is below the given reference line, which illustrates that the linear  
 4 relationship allows reflecting the character of the base metal and welded joints in [26]. Although  
 5 some fatigue experimental FCGR parameters follow the proposed tendency, the correlation curve is  
 6 not suitable to illustrate most of the Paris law parameters of other structural high strength steel.  
 7  
 8  
 9  
 10  
 11  
 12

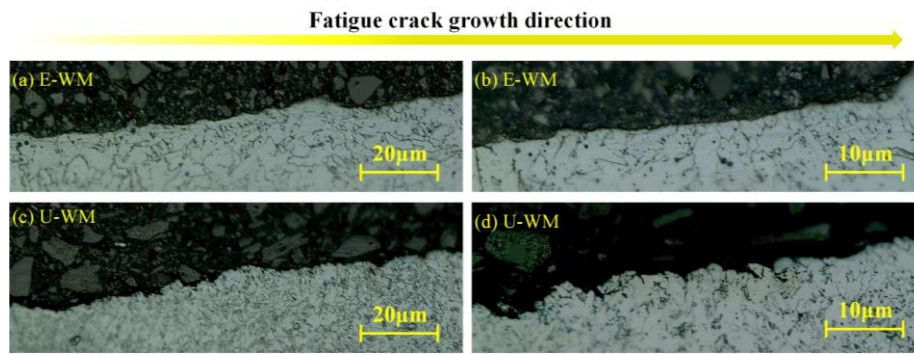


13  
 14  
 15  
 16  
 17  
 18  
 19  
 20  
 21  
 22  
 23  
 24  
 25  
 26  
 27  
 28  
 29  
 30  
 31  
 32 Fig. 12. Correlation of Paris-Erdogen constants  $C$  and  $m$  from literature about different structural  
 33 high strength steel.  
 34  
 35  
 36

### 37 3.6. Fatigue crack path analysis

38 To understand the microstructural mechanism of fatigue fracture, optical microscopy was  
 39 carried on a partial area of E-WM and U-WM fracture paths, cut from a typical intermediate crack  
 40 propagation zone. All fracture samples seem to show a straight crack path by macroscopic  
 41 observation. Fig. 13 shows different scales of optical micrographs of the crack path for E-WM and  
 42 U-WM CT specimens at stress ratio  $R=0.1$ . As can be seen from the comparison between Fig. 13(a)  
 43 and (c), the E-WM overall crack growth path is smoother than that of U-WM. The fracture crack of  
 44 E-WM passes through the mixed bainite and coarse-grained ferrite microstructure region, which  
 45 results in small crack deflection. By contrast, the crack propagates around the pearlite boundary in  
 46 U-WM, which leads to large crack deflection in the local area. It indicates that the pearlite has better  
 47 plastic deformation capability than the mixed microstructure of E-WM. This fracture crack  
 48  
 49  
 50  
 51  
 52  
 53  
 54  
 55  
 56  
 57  
 58  
 59  
 60  
 61  
 62  
 63  
 64  
 65

1 characteristic comparison between E-WM and U-WM is more evident, according to Fig. 13(b) and  
2 (d). The pearlite and ferrite microstructures in U-WM demonstrate more tortuous crack propagation  
3 paths than that of the larger bainite and coarse-grained ferrite grain in E-WM. Furthermore, a  
4 significant difference of FCGR in E-WM and U-WM is reflected in Fig. 10. A similar observation  
5 that the crack tends to propagate along the austenite grain contours is presented by Zhu et al. [18].  
6  
7  
8  
9

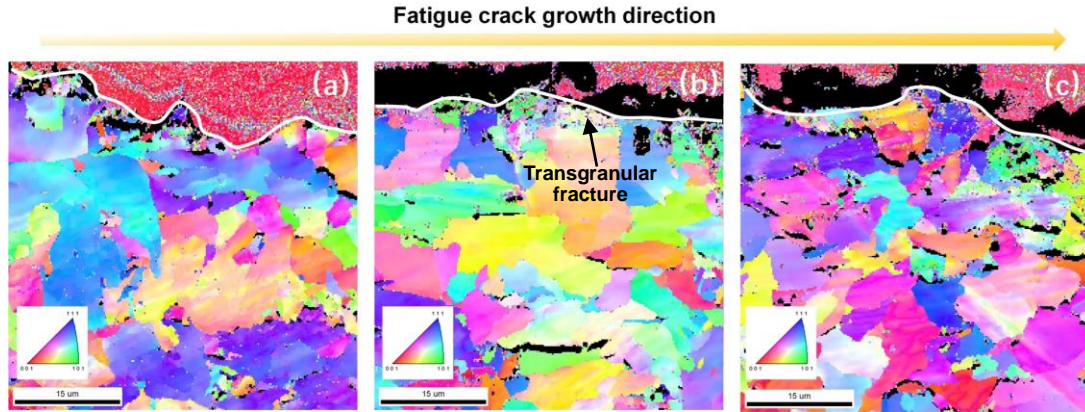


10  
11  
12  
13  
14  
15  
16  
17  
18  
19  
20  
21  
22  
23 Fig. 13. Fatigue crack propagation path for E-WM and U-WM CT specimens at  $R=0.1$  under  
24 different scales.  
25  
26

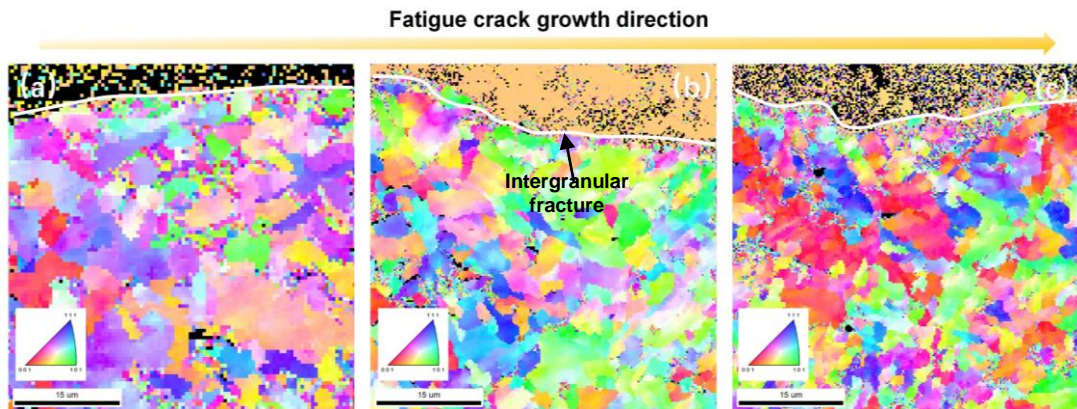
27 Fig. 14 shows the EBSD orientation maps of the crack paths from the cross-section in E-WM  
28 and U-WM specimens at  $R=0.1$ . Fig. 14(a), (b), and (c) represent the fatigue crack initial, stable,  
29 and fast propagation stages in CT specimens, respectively. The three crack growth stages can be  
30 seen when the fatigue cracks along the grain boundaries and passes through the block of bainite  
31 perpendicularly, especially for the stable crack growth stage (Fig. 14(b)). The change of the color a  
32 measure for the origination change, which can be supposed as lattice rotation. Thus, it is implied  
33 that the local microstructures may have undergone a different deformation mode by the variation of  
34 lattice rotation. According to the EBSD observation in Fig. 14(a), the distribution of crystal  
35 orientation along the crack growth shows less variation of misorientation close to the crack-tip in  
36 the initial stage, which illustrates that the microstructural damage derives from the shear  
37 deformation mechanism. On the other hand, the crack branching and secondary cracks near the  
38 crack path are observed at  $R=0.1$  in Fig. 10. Along the FCG path presented in Fig. 14(b) and (c), the  
39 difference of color shows more substantial heterogeneity than Fig. 14(a), which implies significant  
40 plastic deformation during the fatigue crack growth processing. The secondary cracks in the fast  
41 propagation stage (Fig. 14(b)) occur more than the initial and stable crack growth stages.  
42  
43  
44  
45  
46  
47  
48  
49  
50  
51  
52  
53  
54  
55  
56  
57

58 Compared with the E-WM results, the EBSD orientation maps of U-WM are presented in Fig.  
59 15. It can be seen that the grain sizes in U-WM are smaller than the E-WM, and the prominent  
60  
61  
62  
63  
64  
65

1 cracks propagate along the fine grain boundary. Based on the color difference, the crystal orientation  
2 in Fig. 15(a) and (c) show substantial heterogeneity, which illustrates significant plastic deformation  
3 during crack path deflection.  
4  
5  
6



22 Fig. 14. EBSD observation of fatigue crack growth of the E-WM material. (Global FCG direction  
23 is from left to right, and the white lines indicate crack growth paths)  
24

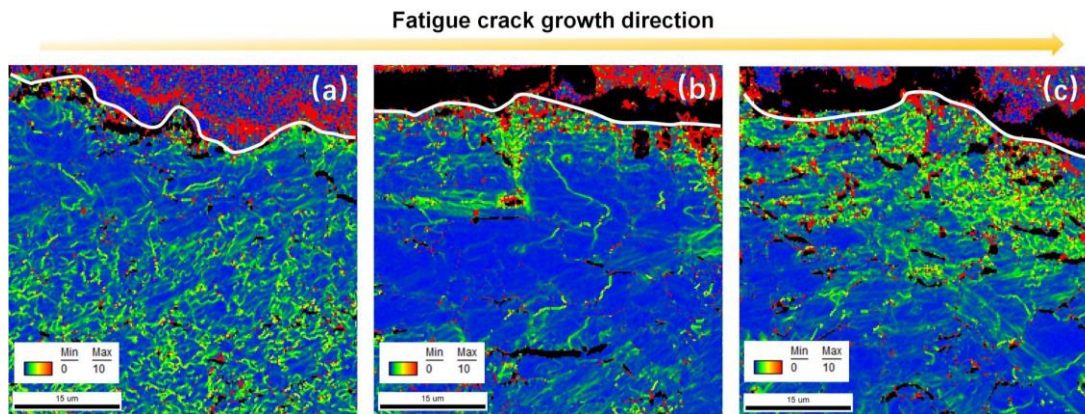


41 Fig. 15. EBSD observation of fatigue crack growth of the U-WM material. (Global FCG direction  
42 is from left to right, and the white lines indicate crack growth paths)  
43

44 To directly compare the deformation mechanisms between the evenmatched welds and  
45 undermatched welds, the Kernel Average Misorientation (KAM) ( $0-10^\circ$ ) investigation on fracture  
46 paths has been performed on E-WM and U-WM CT specimens, which is presented in Fig. 16 and  
47 Fig. 17. Local misorientation is intrinsic lattice defects in GNDs, which is used to judge plastic  
48 deformation mechanism or dislocation motion. It represents the arithmetic average misorientation  
49 of the given pixel versus the neighboring pixels [45]. The local misorientation angle in the vicinity  
50 of the crack path reflects the different degrees of plastic deformation. Fig. 16 shows that the local  
51 inhomogeneous misorientation distribution of crack propagation occurs dominantly near fatigue  
52 crack in E-WM. However, it is worth mentioning that a larger inhomogeneous misorientation area  
53  
54  
55  
56  
57  
58  
59  
60  
61  
62  
63  
64  
65



1 is observed around the crack path in U-WM (Fig. 17) compared with E-WM (Fig. 16), which  
 2 indicated that relatively severe plastic deformation in U-WM (Fig. 17). Thus, it is inferred that the  
 3 U-WM exhibits excellent deformation ability than the E-WM during the fatigue crack propagation.  
 4 In comparison with three different crack growth stages, furthermore, the plastic deformation in the  
 5 crack extension accelerated stage is heavier than the initial and stable stages for both E-WM and U-  
 6 WM. In comparison with three different crack growth stages, furthermore, the plastic deformation in the  
 7 crack extension accelerated stage is heavier than the initial and stable stages for both E-WM and U-  
 8 WM. While the plastic deformation degree in the crack growth stable stage is lower than the other  
 9 two stages.  
 10  
 11  
 12  
 13



14  
 15  
 16  
 17  
 18  
 19  
 20  
 21  
 22  
 23  
 24  
 25  
 26  
 27  
 28  
 29  
 30  
 31  
 32  
 33  
 34  
 35  
 36  
 37  
 38  
 39  
 40  
 41  
 42  
 43  
 44  
 45  
 46  
 47  
 48  
 49  
 50  
 51  
 52  
 53  
 54  
 55  
 56  
 57  
 58  
 59  
 60  
 61  
 62  
 63  
 64  
 65

Fig. 16. The corresponding Kernel Average Misorientation (KAM) maps resulted from EBSD analyses for the E-WM material. (Global FCG direction is from left to right, the white lines indicate crack growth paths)

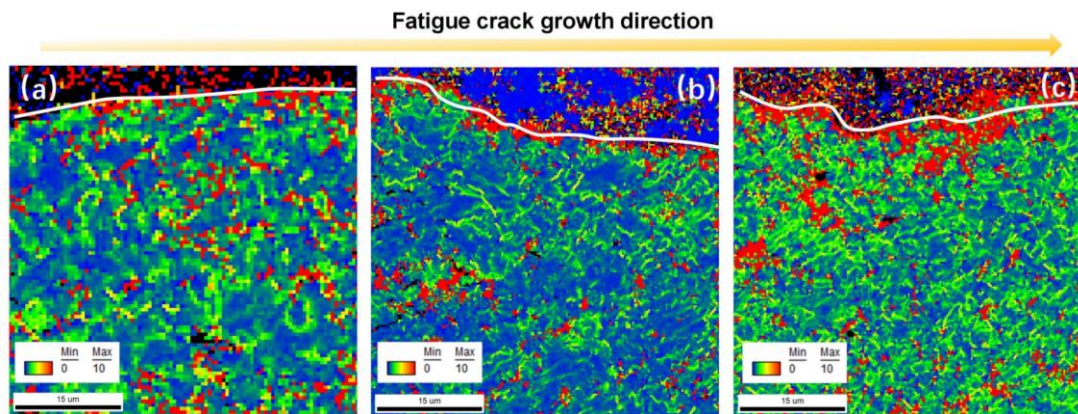


Fig. 17. The corresponding Kernel Average Misorientation (KAM) maps resulted from EBSD analyses for the U-WM material. (Global FCG direction is from left to right, the white lines indicate crack growth paths)

### 3.7. Fatigue fractography analysis

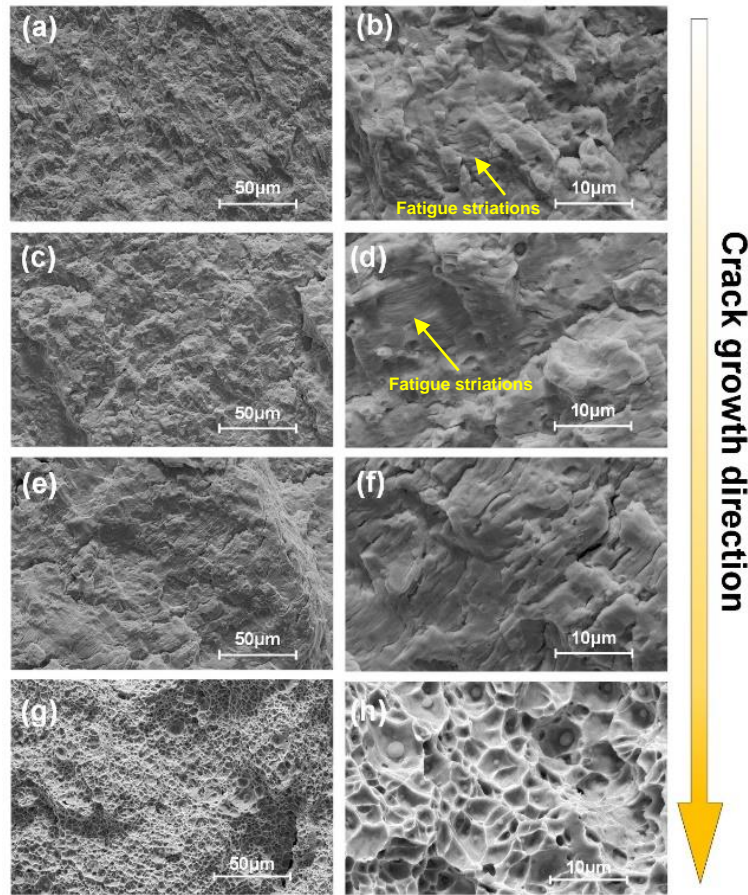
All the tested E-WM and U-WM CT specimens at  $R=0.1$  have been carried on fractography

1 analysis by different scales. The fracture morphologies of E-WM and U-WM specimens under these  
2 regimes by two different specific magnifications (scale bars 10  $\mu\text{m}$  and 50  $\mu\text{m}$ ) are presented in Fig.  
3 18 and Fig. 19, respectively. The crack propagation direction of all the fracture surfaces is marked  
4 from top to bottom, shown as the yellow arrow. It can be seen from Fig. 18 and Fig. 19 in the plotting  
5 scale of 10  $\mu\text{m}$  that the crack growth surface of U-WM has relative rougher fracture surface  
6 morphology than that of E-WM, and fracture paths of U-WM are intergranular and highly tortuous.  
7 Furthermore, flat surfaces are also observed in E-WM local areas, which is suggested to be formed  
8 by transgranular fracture. Thus, E-WM and U-WM demonstrate different fracture mechanisms.  
9

10 The presence of striations provides information for the failure analysis in component service,  
11 the global and local propagation direction, and crack growth rate [46, 47]. The presence of fatigue  
12 striations characteristic results from the blunt plastic process at the crack tip [48]. To demonstrate  
13 the striations of the fracture surface for different specimens, the local fracture surfaces in different  
14 regimes are captured in Fig. 18 and Fig. 19. According to the typical fractography of E-WM (Fig.  
15 18), many parallel fatigue striations and edges nearly perpendicular to the crack propagation  
16 direction were observed in different growth regimes. The distance between striations in E-WM is  
17 gradually more extensive from the initial crack regime to the accelerated growth regime. Generally,  
18 the fatigue striations and existed edges are related to the level of  $\Delta K$ . However, the fatigue striations  
19 were not exhibited obviously. Only in the accelerated growth regimes shows the fatigue striation  
20 marks slightly. The different characteristic appearance of striation morphology is dependent on the  
21 material microstructures. Moreover, several short secondary microcracks can be observed clearly  
22 beneath the fracture surface in different regimes. Compared with U-WM in Fig. 19, few tiny  
23 secondary microcracks perpendicular to the direction of crack growth exist in the accelerated growth  
24 regime in fracture surfaces of BM specimens.  
25

26 The comparison between fracture morphologies of E-WM and U-WM in the final failure  
27 regime is shown by Fig. 19 (g) (h) and Fig. 19 (g) (h). Substantial dimples can be seen on the fracture  
28 surfaces for these two materials, which indicate a ductile fracture mechanism induced by micro-  
29 void coalescence. The dimples on the fracture surface of the E-WM specimen are deeper than the  
30 U-WM specimen, showing typical ductile fracture morphology for metallic materials. It further  
31 indicates E-WM has stronger plastic deformation ability than the U-WM. It should be noticed that  
32 plenty of secondary particles in the E-WM fracture surface were shown in Fig. 19(h). The ductile  
33  
34  
35  
36  
37  
38  
39  
40  
41  
42  
43  
44  
45  
46  
47  
48  
49  
50  
51  
52  
53  
54  
55  
56  
57  
58  
59  
60  
61  
62  
63  
64  
65

1 fracture surface of the final stage was scanned and analyzed by Energy Dispersive Spectrometry  
2 (EDS). The scanning spots and energy spectra are shown in Fig. 20. The EDS results indicate that  
3 the particles are mainly Ti-rich inclusions, which possibly came from the weld filler during the  
4 cooling stage of the welding process.  
5  
6  
7



39 Fig. 18. Typical fractography of E-WM specimens under different regimes by different scales (10  
40  $\mu\text{m}$  and 50  $\mu\text{m}$ ). (a) and (b) initial crack growth regime, (c) and (d) intermediate growth regime,  
41  
42 (e) and (f) accelerated growth regime, (g) and (h) ductile fracture zone.  
43  
44  
45  
46  
47  
48  
49  
50  
51  
52  
53  
54  
55  
56  
57  
58  
59  
60  
61  
62  
63  
64  
65

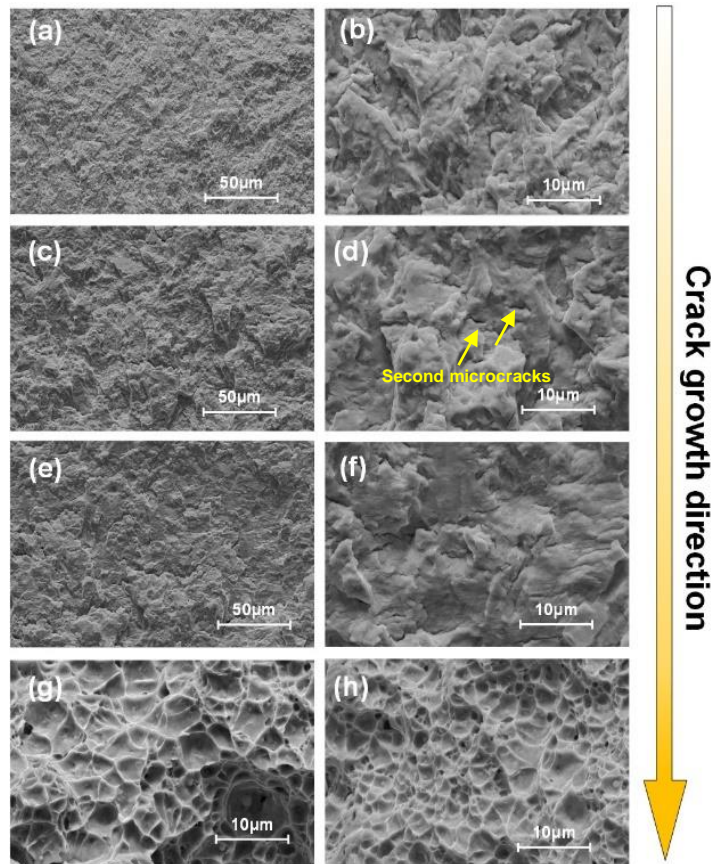


Fig. 19. Typical fractography of U-WM specimens under different regimes by different scales (10  $\mu\text{m}$  and 50  $\mu\text{m}$ ). (a) and (b) initial crack growth regime, (c) and (d) intermediate growth regime, (e) and (f) accelerated growth regime, (g) and (h) ductile fracture zone.

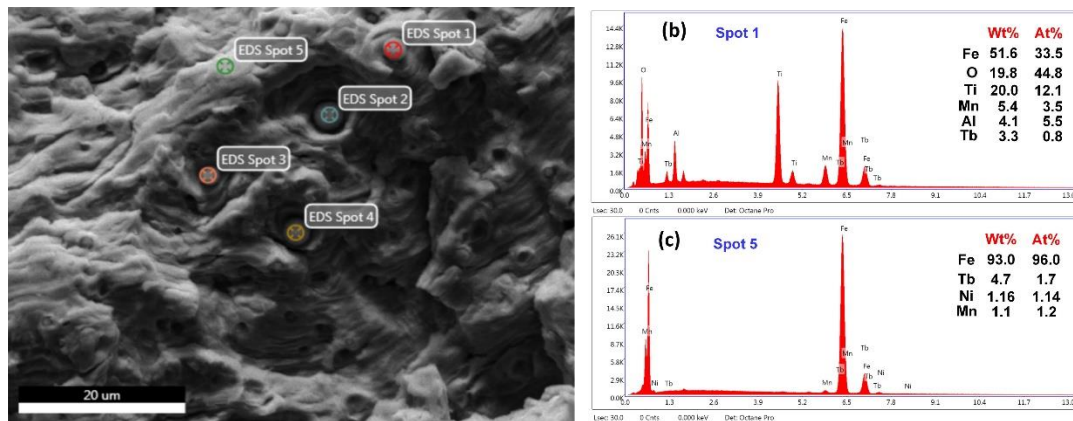


Fig. 20. (a) SEM image of a secondary particle on the fracture surface of the E-WM and (b) EDS profiles of the particle. (c) EDS profiles of base metal.

### 3.8 Discussion

To apply the fatigue properties for the fatigue reliability assessment of engineering structures, the relationship between the fatigue properties and welded joints geometries should be clarified. On the

1 one hand, the fatigue crack growth properties for BM and weldments can be employed to predict  
2 the fatigue propagation life for different welded joints or complex welded components [22, 49]. A  
3 low cycle fatigue based FCG model could be used to predict the long and physically short crack,  
4 and further expended to realize the fatigue life prediction of components for engineering  
5 applications [50]. Combined with the fatigue reliability theory, some deficiency of computational  
6 results with conventional fatigue assessment approaches would be examined considering various  
7 effects on the basis of notch concept in HCF regimes, such as the weldment random geometrical  
8 details, residual stress effect [51], fatigue loading conditions, service conditions [52], crack  
9 propagation threshold and misalignment [53, 54]. On the other hand, the fatigue properties of  
10 materials in LCF regime can be utilized to estimate the fatigue initiation life under different fatigue  
11 loading modes. Under the stress-controlled loading mode, the ratchetting-fatigue interaction could  
12 be illustrated by ductility exhaustion theory and continuum damage mechanics [55]. The cyclic  
13 soften or hardening behavior is also significant effect in LCF assessment of the welded joints [56].  
14 Thus, the fatigue properties of materials in LCF regime are the substantial parameters to estimate  
15 the fatigue life of welded joints and components.  
16  
17  
18  
19  
20  
21  
22  
23  
24  
25  
26

#### 27 **4. Conclusions:**

28  
29  
30  
31  
32 The present paper studies fatigue crack growth behavior of 10CrNi3MoV high strength steel  
33 evenmatched (E-WM) and undermatched (U-WM) weldments by different characteristic methods.  
34 The effects of microstructure, welding residual stress and stress ratio were analyzed and discussed.  
35  
36 Based on the above studies, the following conclusions are drawn:  
37  
38  
39

- 40 (1) For the low  $R$ -ratio ( $R=0.1$ ), the U-WM demonstrates higher FCGR curves than that in the  
41 BM and E-WM. The carbides in mixed pearlite and ferrite microstructure exhibits lower  
42 fatigue crack growth resistance than the mixed bainite and ferrite microstructures of E-WM.  
43 Ti-rich inclusion in E-WM can be beneficial to stimulate the nucleation of acicular ferrite  
44 and further elevate the fatigue crack growth resistance. Besides, there is no significant  
45 difference of FCGR for E-WM and U-WM between high  $R$ -ratios (0.4 and 0.7).  
46  
47  
48  
49  
50  
51  
52 (2) Two different fracture mechanisms are exhibited for E-WM and U-WM. Transgranular  
53 fracture appearances were shown on E-WM, while the intergranular fracture surfaces were  
54 observed on U-WM. Plenty of secondary particles in the E-WM fracture surface exist, while  
55 few tiny secondary microcracks perpendicular to the direction of crack growth are observed  
56  
57  
58  
59  
60  
61  
62  
63  
64  
65

1 in the U-WM accelerated growth regime, indicating that the U-WM has better ductility than  
2 E-WM.  
3

- 4 (3) The FCGR of base metal and weldments have been evaluated under as-welded and PWHT.  
5  
6 The results demonstrate that residual stress in the extracted CT specimens has noticeably  
7 influenced the FCGR of E-WM and U-WM. Regarding the E-WM specimens, the FCGR in  
8 the as-welded state is less than in the PWHT state due to compressive residual stresses. As  
9 for U-WM specimens at  $R=0.1$  and  $0.4$ , FCGR under the as-welded state is slightly lower  
10 than PWHT state, attributing to the tensile residual stress effect on fatigue crack tip.  
11  
12 (4) According to the KAM analysis, the plastic deformation in the crack extension accelerated  
13 regime is heavier than the initial and stable stages for both E-WM and U-WM by  
14 comparison with three different crack growth regimes. More advanced characterization  
15 methods may be applied to study the fundamental mechanism of the material heterogeneity  
16 cracking phenomena in the future.  
17  
18  
19  
20  
21  
22  
23  
24  
25  
26  
27  
28

## 29 **Statements of Contribution**

30

31  
32 Wei Song and Xuesong Liu together proposed this methodology. Wei Song did finite element  
33 analysis and calculations. Ping Wang helped to study and explain the experimental data. Di Wan  
34 helped to illustrate the microstructure mechanism of fatigue fracture in the paper. Filippo Berto  
35 supervised the findings of this work. Guian Qian and José Correia revised the manuscript. All  
36 authors discussed the results and contributed to the final manuscript.  
37  
38  
39  
40  
41  
42  
43

## 44 **Acknowledgements :**

45

46  
47  
48 The research project is supported by the Natural Science Foundation of Jiangsu Province (grant no.  
49 BK20200174), the Natural Science Foundation of the Higher Education Institutions of Jiangsu  
50 Province (grant no. 20KJB430008), and the Qinglan Project in Jiangsu Province.  
51  
52  
53  
54  
55  
56  
57  
58  
59  
60  
61  
62  
63  
64  
65

## Reference:

- 1  
2  
3  
4  
5 [1] J. Venezuela, Q. Zhou, Q. Liu, H. Li, M. Zhang, M.S. Dargusch, A. Atrens, The influence of  
6  
7 microstructure on the hydrogen embrittlement susceptibility of martensitic advanced high  
8  
9 strength steels, *Materials Today Communications*, 17 (2018) 1-14.  
10  
11  
12 [2] Q. Liu, Q. Zhou, J. Venezuela, M. Zhang, J. Wang, A. Atrens, A review of the influence of  
13  
14 hydrogen on the mechanical properties of DP, TRIP, and TWIP advanced high-strength steels  
15  
16 for auto construction, *Corrosion Reviews*, 34 (2016) 127-152.  
17  
18  
19 [3] J. Venezuela, Q. Liu, M. Zhang, Q. Zhou, A. Atrens, A review of hydrogen embrittlement of  
20  
21 martensitic advanced high-strength steels, *Corrosion Reviews*, 34 (2016) 153-186.  
22  
23  
24 [4] S.K. Dwivedi, M. Vishwakarma, Effect of hydrogen in advanced high strength steel materials,  
25  
26  
27 *International Journal of Hydrogen Energy*, 44 (2019) 28007-28030.  
28  
29  
30 [5] S. Takagi, Y. Toji, M. Yoshino, K. Hasegawa, Hydrogen Embrittlement Resistance  
31  
32 Evaluation of Ultra High Strength Steel Sheets for Automobiles, *ISIJ International*, 52 (2012)  
33  
34  
35 316-322.  
36  
37  
38 [6] O. Todoshchenko, Y. Yagodzinsky, V. Yagodzinska, T. Saukkonen, H. Hänninen,  
39  
40  
41 Hydrogen effects on fracture of high-strength steels with different micro-alloying, *Corrosion*  
42  
43  
44 *Reviews*, 33 (2015) 515-527.  
45  
46  
47 [7] C.M. Younes, A.M. Steele, J.A. Nicholson, C.J. Barnett, Influence of hydrogen content on  
48  
49  
50 the tensile properties and fracture of austenitic stainless steel welds, *International Journal of*  
51  
52  
53 *Hydrogen Energy*, 38 (2013) 4864-4876.  
54  
55  
56 [8] J.J. Hoyos, M. Masoumi, V.F. Pereira, A.P. Tschiptschin, M.T.P. Paes, J.A. Avila, Influence  
57  
58  
59 of hydrogen on the microstructure and fracture toughness of friction stir welded plates of API  
60  
61  
62  
63  
64  
65

1 5L X80 pipeline steel, International Journal of Hydrogen Energy, 44 (2019) 23458-23471.

2  
3 [9] D.M. Viano, N.U. Ahmed, G.O. Schumann, Influence of heat input and travel speed on  
4  
5  
6 microstructure and mechanical properties of double tandem submerged arc high strength low  
7  
8  
9 alloy steel weldments, Science and Technology of Welding and Joining, 5 (2000) 26-34.

10  
11 [10] L.H.S. Barbosa, P.J. Modenesi, L.B. Godefroid, A.R. Arias, Fatigue crack growth rates on  
12  
13  
14 the weld metal of high heat input submerged arc welding, International Journal of Fatigue, 119  
15  
16  
17 (2019) 43-51.

18  
19 [11] X. Liu, K.-F. Chung, H.-C. Ho, M. Xiao, Z.-X. Hou, D.A. Nethercot, Mechanical behavior of  
20  
21  
22 high strength S690-QT steel welded sections with various heat input energy, Engineering  
23  
24  
25 Structures, 175 (2018) 245-256.

26  
27 [12] Y. Zhai, B. Huang, Z. Zhang, X. Mao, Z. Zhao, Effect of preheating on welding cold crack  
28  
29  
30 sensitivity of China low activation martensitic steel, Fusion Engineering and Design, 133 (2018)  
31  
32  
33 32-38.

34  
35 [13] T. Dai, J.C. Lippold, The effect of postweld heat treatment on hydrogen-assisted cracking  
36  
37  
38 of 8630/Alloy 625 overlay, Welding in the World, 62 (2018) 581-599.

39  
40 [14] M.C. Zhao, K. Yang, Y. Shan, The effects of thermo-mechanical control process on  
41  
42  
43 microstructures and mechanical properties of a commercial pipeline steel, Materials Science  
44  
45  
46 and Engineering A, 335 (2002) 14-20.

47  
48 [15] Y. Xiong, X.X. Hu, The effect of microstructures on fatigue crack growth in Q345 steel  
49  
50  
51 welded joint, Fatigue and Fracture of Engineering Materials and Structures, 35 (2012) 500-512.

52  
53 [16] Z. Xiong, S. Liu, X. Wang, C. Shang, X. Li, R.D.K. Misra, The contribution of intragranular  
54  
55  
56 acicular ferrite microstructural constituent on impact toughness and impeding crack initiation  
57  
58  
59

60  
61  
62  
63  
64  
65



1 and propagation in the heat-affected zone (HAZ) of low-carbon steels, *Materials Science and*  
2  
3 *Engineering A*, 636 (2015) 117-123.

4  
5  
6 [17] Q. Wang, Z. Yan, X. Liu, Z. Dong, H. Fang, Understanding of fatigue crack growth behavior  
7  
8 in welded joint of a new generation Ni-Cr-Mo-V high strength steel, *Engineering Fracture*  
9  
10 *Mechanics*, 194 (2018) 224-239.

11  
12  
13 [18] M.-L. Zhu, F.-Z. Xuan, G.-Z. Wang, Effect of microstructure on fatigue crack propagation  
14  
15 behavior in a steam turbine rotor steel, *Materials Science and Engineering: A*, 515 (2009) 85-  
16  
17  
18  
19  
20 92.

21  
22 [19] S.-D. Liu, M.-L. Zhu, H.-B. Zhou, D. Wan, F.-Z. Xuan, Strain visualization of growing short  
23  
24 fatigue cracks in the heat-affected zone of a Ni-Cr-Mo-V steel welded joint: Intergranular  
25  
26 cracking and crack closure, *International Journal of Pressure Vessels and Piping*, 178 (2019)  
27  
28  
29  
30 103992.

31  
32 [20] J.A. Ronevich, E. Ju Song, Z. Feng, Y. Wang, C. D'Elia, M.R. Hill, Fatigue crack growth  
33  
34 rates in high pressure hydrogen gas for multiple X100 pipeline welds accounting for crack  
35  
36 location and residual stress, *Engineering Fracture Mechanics*, (2019) 106846.

37  
38 [21] S. Li, Y. Kang, G. Zhu, S. Kuang, Microstructure and fatigue crack growth behavior in  
39  
40 tungsten inert gas welded DP780 dual-phase steel, *Materials & Design*, 85 (2015) 180-189.

41  
42 [22] L. Zong, G. Shi, Y. Wang, Experimental investigation and numerical simulation on fatigue  
43  
44 crack behavior of bridge steel WNQ570 base metal and butt weld, *Construction and Building*  
45  
46 *Materials*, 77 (2015) 419-429.

47  
48 [23] A.M.P. de Jesus, R. Matos, B.F.C. Fontoura, C. Rebelo, L. Simões da Silva, M. Veljkovic,  
49  
50 A comparison of the fatigue behavior between S355 and S690 steel grades, *Journal of*  
51  
52  
53  
54  
55  
56  
57  
58  
59  
60  
61  
62  
63  
64  
65

1           Constructional Steel Research, 79 (2012) 140-150.

2  
3           [24] J. Lukács, Á. Dobosy, Matching effect on fatigue crack growth behaviour of high-strength  
4  
5  
6           steels GMA welded joints, Welding in the World, 63 (2019) 1315-1327.

7  
8  
9           [25] C. Zhang, P. Lu, X. Hu, X. Song, Residual stress-induced deformation and fatigue crack  
10  
11           growth in weld-repaired high-strength low-alloy steel with soft buffer layer, Materials Science  
12  
13           and Engineering: A, 564 (2013) 147-157.

14  
15  
16  
17           [26] A. Mehmanparast, F. Brennan, I. Tavares, Fatigue crack growth rates for offshore wind  
18  
19           monopile weldments in air and seawater: SLIC inter-laboratory test results, Materials & Design,  
20  
21           114 (2017) 494-504.

22  
23  
24  
25           [27] W. Yun, B. Philip, X. Zhenying, W. Junfeng, Study on fatigue crack growth performance of  
26  
27           EH36 weldments by laser shock processing, Surfaces and Interfaces, 15 (2019) 199-204.

28  
29  
30           [28] X. Huang, T. Moan, Improved modeling of the effect of R-ratio on crack growth rate,  
31  
32           International Journal of Fatigue, 29 (2007) 591-602.

33  
34  
35  
36           [29] Y. Li, H. Wang, D. Gong, The interrelation of the parameters in the Paris equation of fatigue  
37  
38           crack growth, Engineering Fracture Mechanics, 96 (2012) 500-509.

39  
40  
41           [30] K. Sadananda, A.K. Vasudevan, Fatigue crack growth mechanisms in steels, International  
42  
43           Journal of Fatigue, 25 (2003) 899-914.

44  
45  
46  
47           [31] R.C. McClung, The influence of applied stress, crack length, and stress intensity factor on  
48  
49           crack closure, Metallurgical Transactions A, 22 (1991) 1559-1571.

50  
51  
52           [32] J.C. Newman Jr, A crack opening stress equation for fatigue crack growth, International  
53  
54           Journal of Fracture, 24 (1984) R131-R135.

55  
56  
57  
58           [33] A.J. McEvily, R.O. Ritchie, Crack closure and the fatigue-crack propagation threshold as a  
59  
60  
61  
62  
63  
64  
65

1 function of load ratio, *Fatigue and Fracture of Engineering Materials and Structures*, 21 (1998)  
2  
3 847-855.

4  
5  
6 [34] A. Jacob, A. Mehmanparast, R. D'Urzo, J. Kelleher, Experimental and numerical  
7  
8 investigation of residual stress effects on fatigue crack growth behaviour of S355 steel  
9  
10 weldments, *International Journal of Fatigue*, 128 (2019) 105196.

11  
12  
13 [35] K.S. Ravi Chandran, S.E. Galyon Dorman, The nature of specimen-size-effect on fatigue  
14  
15 crack growth and net-section fracture mechanics approach to extract the size-independent  
16  
17 behavior, *International Journal of Fatigue*, 145 (2021) 106088.

18  
19  
20 [36] B. Tabernig, P. Powell, R. Pippan, *Fatigue Crack Growth Thresholds, Endurance Limits,*  
21  
22 *and Design*, (2000).

23  
24  
25 [37] S.C. Forth, J.C. Newman Jr, R.G. Forman, Anomalous fatigue crack growth data generated  
26  
27 using the ASTM standards, in: *ASTM Special Technical Publication*, 2007, pp. 244-255.

28  
29  
30 [38] W. Song, X. Liu, F. Berto, S.M.J. Razavi, Low-Cycle Fatigue Behavior of 10CrNi3MoV High  
31  
32 Strength Steel and Its Undermatched Welds, *Materials (Basel)*, 11 (2018) 661.

33  
34  
35 [39] B.S. Institution, *Metallic materials - Fatigue testing - Fatigue crack growth method*, in: *BS*  
36  
37 *ISO 12108:2012*, London, 2012.

38  
39  
40 [40] H.X. Yuhang Lou, Yun Peng, Study on microstructure and properties of welded joints of a  
41  
42 690 MPa grade HSLA steel, *Materials Science and Technology*, 20 (2012) 101-107.

43  
44  
45 [41] A.R. Shahani, I. Shakeri, Experimental evaluation of fatigue behaviour of thin Al5456  
46  
47 welded joints, *Fatigue & Fracture of Engineering Materials & Structures*, 43 (2020) 965-977.

48  
49  
50 [42] A.F. Hobbacher, *Recommendations for Fatigue Design of Welded Joints and Components*,  
51  
52 *IIW Collection*, in: *Recommendations for Fatigue Design of Welded Joints and Components*,

53  
54  
55  
56  
57  
58  
59  
60  
61  
62  
63  
64  
65

1 London, 2016.

2  
3 [43] S. Huang, J.Z. Zhou, J. Sheng, K.Y. Luo, J.Z. Lu, Z.C. Xu, X.K. Meng, L. Dai, L.D. Zuo,  
4  
5  
6 H.Y. Ruan, H.S. Chen, Effects of laser peening with different coverage areas on fatigue crack  
7  
8  
9 growth properties of 6061-T6 aluminum alloy, *International Journal of Fatigue*, 47 (2013) 292-  
10  
11  
12 299.

13  
14 [44] M. Pavan, D. Furfari, B. Ahmad, M.A. Gharghour, M.E. Fitzpatrick, Fatigue crack growth  
15  
16  
17 in a laser shock peened residual stress field, *International Journal of Fatigue*, 123 (2019) 157-  
18  
19  
20 167.

21  
22 [45] Z. Zhang, H. Ma, R. Zheng, Q. Hu, M. Nakatani, M. Ota, G. Chen, X. Chen, C. Ma, K.  
23  
24  
25 Ameyama, Fatigue behavior of a harmonic structure designed austenitic stainless steel under  
26  
27  
28 uniaxial stress loading, *Materials Science and Engineering: A*, 707 (2017) 287-294.

29  
30 [46] N.W. Sachs, Understanding the surface features of fatigue fractures: how they describe  
31  
32  
33 the failure cause and the failure history, *J. Fail. Anal. Prev.*, 5 (2005) 11-15.

34  
35  
36 [47] J. Schijve, *Fatigue as a phenomenon in the material*, Springer, 2001.

37  
38  
39 [48] S. Suresh, *Fatigue of Materials*, 2004.

40  
41  
42 [49] L. Zong, G. Shi, Y.Q. Wang, Z.X. Li, Y. Ding, Experimental and numerical investigation on  
43  
44  
45 fatigue performance of non-load-carrying fillet welded joints, *Journal of Constructional Steel*  
46  
47  
48 *Research*, 130 (2017) 193-201.

49  
50 [50] S.C. Wu, Z.W. Xu, C. Yu, O.L. Kafka, W.K. Liu, A physically short fatigue crack growth  
51  
52  
53 approach based on low cycle fatigue properties, *International Journal of Fatigue*, 103 (2017)  
54  
55  
56 185-195.

57  
58 [51] H. Xin, J.A.F.O. Correia, M. Veljkovic, F. Berto, L. Manuel, Residual stress effects on  
59  
60  
61  
62  
63  
64  
65

1 fatigue life prediction using hardness measurements for butt-welded joints made of high  
2  
3 strength steels, *International Journal of Fatigue*, 147 (2021) 106175.  
4

5  
6 [52] Y. Hu, S. Wu, P.J. Withers, H. Cao, P. Chen, Y. Zhang, Z. Shen, T. Vojtek, P. Hutař,  
7  
8 Corrosion fatigue lifetime assessment of high-speed railway axle EA4T steel with artificial  
9  
10 scratch, *Engineering Fracture Mechanics*, 245 (2021) 107588.  
11  
12

13  
14 [53] Y. Dong, Y. Garbatov, C. Guedes Soares, Strain-based fatigue reliability assessment of  
15  
16 welded joints in ship structures, *Marine Structures*, 75 (2021) 102878.  
17  
18

19  
20 [54] Y. Dong, Y. Garbatov, C. Guedes Soares, Improved effective notch strain approach for  
21  
22 fatigue reliability assessment of load-carrying fillet welded cruciform joints in low and high cycle  
23  
24 fatigue, *Marine Structures*, 75 (2021).  
25  
26

27  
28 [55] H. Luo, G. Kang, Q. Kan, A low-cycle fatigue life-prediction model for SUS301L stainless  
29  
30 steel butt-welded joint with considering ratchetting, *International Journal of Fatigue*, 139 (2020)  
31  
32 105777.  
33  
34

35  
36 [56] W. Song, X. Liu, F. Berto, S.M.J. Razavi, Energy-based low cycle fatigue indicator  
37  
38 prediction of non-load-carrying cruciform welded joints, *Theoretical and Applied Fracture*  
39  
40 *Mechanics*, 96 (2018) 247-261.  
41  
42  
43  
44  
45  
46  
47  
48  
49  
50  
51  
52  
53  
54  
55  
56  
57  
58  
59  
60  
61  
62  
63  
64  
65

The authors declare that they have no known competing financial interests or personal relationships that could have appeared to influence the work reported in this paper.